Spring 2018

Determination of the Oxidative Capacity of Soot Toward GSH and Characterization of Soot Physicochemical Properties

Kaylee Troth
Central Washington University, kayleetroth@gmail.com

Determination of the Oxidative Capacity of Soot Toward GSH and Characterization of Soot Physicochemical Properties

---

A Thesis

Presented to

The Graduate Faculty

Central Washington University

In Partial Fulfillment

of the Requirements for the Degree

Master of Science

Chemistry

---

by Kaylee Marie Troth

May 2018

CENTRAL WASHINGTON UNIVERSITY

Graduate Studies

We hereby approve the thesis of

Kaylee Marie Troth

Candidate for the degree of Master of Science

APPROVED FOR THE GRADUATE FACULTY

5/23/2018

Dr. Anne Johansen, Committee Chair

5/24/18

Dr. Dion Rivera

5/22/2018

Dr. Tim Sorey

Dean of Graduate Studies

ABSTRACT

Fine atmospheric particulate matter ($PM_{2.5}$) emitted during the combustion of fossil and biomass fuels is known to adversely affect human health. While the underlying mechanisms are thought to be driven by the generation of reactive oxygen species (ROS), specific particle characteristics responsible for this detrimental effect are not well understood. In this research, the quantitative determination of the biologically relevant antioxidant, glutathione (GSH), was optimized for use as an indicator of oxidative stress to shed light on relevant particle characteristics. This was accomplished via fluorescent spectroscopy for GSH determination by way of reaction with *o*-phthalaldehyde (OPA), a fluorescent marker. Physicochemical properties of particles were studied using Scanning Electron Microscopy (SEM), laser particle size analyzer, Inductively Coupled Plasma Mass Spectrometry (ICP-MS), and Thermal Gravimetric Analysis (TGA) to determine particle morphology, aqueous particle surface area and diameter, trace metal content, and volatile organic content, respectively. These physical and chemical properties were correlated with the oxidative capacity of particles in reaction with GSH. Results show that the fluorometric analysis of GSH is relatively simple to employ to study particle toxicity and that different particles display unique oxidative capacity, which cannot be directly correlated to any one of the measured parameters. The pseudo first order rate constant, k', for heat-treated samples was correlated to total transition metals and the loss of mass after heat treatment to 700 $^{\circ}$C with an R^2 value of 0.708. It is thought that elemental carbon (EC) drives particle toxicity. This research contributes to the analytical determination of particle toxicity and helps increase our understanding of the mechanisms that control their adverse effects.

TABLE OF CONTENTS

LIST OF TABLES

LIST OF FIGURES

CHAPTER I

INTRODUCTION AND LITERATURE REVIEW

Fine particulate matter ($PM_{2.5}$) are particles < 2.5 µm in diameter generated from the combustion of fossil or biomass fuels. $PM_{2.5}$ contains a variety of substances such as organics, inorganics, sulfites, and dust. Toxicity of $PM_{2.5}$ has been well studied in recent years as particles have been found to have a negative impact on human and environmental health (*Bell et al.,* 2009; *Jacobson et al.,* 2010). Determination of what causes $PM_{2.5}$ to be toxic has led to studies focusing on a major component of PM, carbon nanoparticles (CNP) which also contain soot (*Cho et al.,* 2005; *McWhinney et al.,* 2013; *Ristovski et al.,* 2012). CNP are linked carbonaceous particles that are nanometer in size and generally spherical in shape. Anthropogenic activities associated with energy consumption such as home heating and transportation are the primary sources of soot production (*Grahame et al.,* 2014). While health effects such as cardiovascular, respiratory, and pulmonary diseases have been linked to CNP particles, the detailed mechanisms and particle characteristics that cause cellular damage are still widely unknown (*Bell et al.,* 2009; *Niranjan et al.,* 2017).

Many studies have focused on diesel PM when looking at exposure in relation to health impacts due to the contribution that diesel traffic has on air quality. Diesel vehicles are used for 94% of goods being transported across the United States and are estimated to use approximately 4 million barrels of diesel as a daily average (*Sharma et al.,* 2012). Studies conducted to quantify soot emissions from diesel vehicles in different locations have shown that diesel emissions in the U.S. amount to 637,167 thousand tons annually (EPA, 2002; *Liggio et al.,* 2012).

While a large body of evidence from epidemiological studies have established the overall negative impact of PM inhalation on respiratory, cardiovascular, and pulmonary health more information is sought on the chemical and physical properties of particles that drive particulate toxicity (*Bell et al.*, 2009; *Brook et al.*, 2010; *Niranjan et al.*, 2017; *Penn et al.*, 2005; *Sharma et al.*, 2012; *Verma et al.*, 2014). To accomplish this, cellular and acellular methods have been developed that range in degree of complexity. Motivation for acellular methods that allow for a measure of the oxidative capacity of soots in a simplified acellular system lies in the high-throughput potential and in the fact that complex biological response mechanisms are absent. It is thought that CNP particles are responsible for cellular damage by undergoing redox chemistry where reactive oxygen species (ROS) are generated. ROS include superoxide radical ($\cdot O_2^-$), hydrogen peroxide (H_2O_2), hydroperoxyl radical ($HO_2\cdot$), and hydroxyl radical ($\cdot OH$) (*Glausauer and Chandel,* 2013*)*. Equations 1 through 5 show how the various ROS species are transformed and related.

$$O_2 \xrightarrow[-0.33\ V]{e^-} \cdot O_2^- \qquad \text{Eqn. 1}$$

$$\cdot O_2^- \xrightarrow[+0.89\ V]{e^- + 2H^+} H_2O_2 \qquad \text{Eqn. 2}$$

$$H_2O_2 \xrightarrow[+0.38\ V]{e^-} \cdot OH + OH^- \qquad \text{Eqn. 3}$$

$$\cdot OH + OH^- \xrightarrow[+2.32\ V]{e^- + 2H^+} 2\ H_2O \qquad \text{Eqn. 4}$$

$$O_2 \xrightarrow[+0.281\ V]{2e^- + 2H^+} H_2O_2 \qquad \text{Eqn. 5}$$

The equations above indicate the half-cell potential for ROS at a pH of 7 (*Wood,* 1988). ROS can be transformed by electron transfer, with some transformations being more energetically favorable (*Wood,* 1988). It is important to understand that while the production of H_2O from O_2 is more energetically favorable than the production of H_2O_2, the production of H_2O requires a transfer of four electrons and the production of H_2O_2 requires a transfer of only two electrons. Therefore, H_2O_2 is produced in more abundance than H_2O from O_2. ROS are

known to cause cellular damage and stress by oxidation of antioxidants responsible for cellular health (*Glausauer and Chandel,* 2013; *McWhinney et al.*, 2013; *Verma et al.*, 2014).

To investigate the role of CNP as an oxidative agent, the dithiotreitol (DTT) assay is a widely used method to measure the oxidative capacity that particles have on a reducing agent, DTT in this case (*Cho et al.,* 2005; *McWhinney et al.,* 2013; *Tuet et al.,* 2017; *Verma et at.,* 2014). The DTT assay depends on the reaction of particles oxidizing the thiol group on DTT, which then goes on to react with Ellman's reagent (5,5-dithio-bis-2-nitrobenzoic acid, DTNB), generating 5-thio-2-nitrobenzoic acid (TNB). TNB can be detected via UV-Vis spectroscopy with a maximum absorbance at 412 nm at pH 8.0 (*Cho et al.,* 2005).

In the present study, a biologically relevant antioxidant, glutathione (GSH), was chosen as an alternate reducing agent to study the oxidative capacity of surrogate soot particles. GSH is responsible for cellular health and maintenance by converting peroxides to water (*Watson et al.*, 2002). Three amino acids (glutamate, cysteine, and glycine) make up the thiol-containing tripeptide (Figure 1) (*Galant et al.,* 2009; *Millis et al.,* 1988). GSH is the most abundant antioxidant in cells with concentrations of about 100 μM on average (*Galant et al.,* 2009).

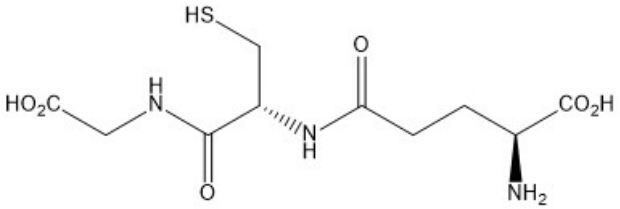

Figure 1. Chemical structure of GSH, a tripeptide antioxidant responsible for maintaining cellular health.

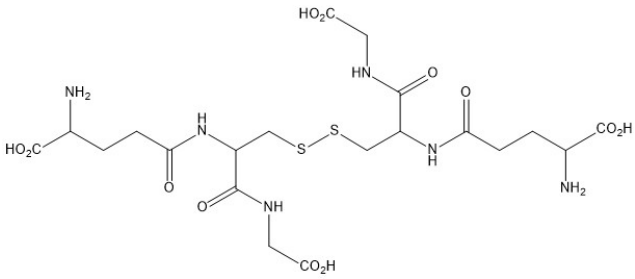

Figure 2. Chemical structure of GSSG.

As in the DTT assay, GSH is determined in the presence of PM to assess oxidative capacity. The method of fluorescence spectroscopy detection is based on GSH reacting with *o*-

phthalaldehyde (OPA) to form a GSH-OPA adduct that fluoresces with an excitation wavelength of 340 nm and an emission wavelength of 420 nm (*Cohn and Lyle,* 1966; *Hissin and Hilf,* 1976; *Roušar et al.,* 2012). When GSH is oxidized, it can form a disulfide bond with another oxidized GSH molecule to form glutathione disulfide (GSSG) (Figure 2). To the best of our knowledge, GSH determination with OPA via fluorescence spectroscopy to determine oxidative capacity has not been used on PM.

GSH was chosen as the antioxidant of interest due to its abundance in the cells. DTT on the other hand is not present in cells, nor is it representative of a cellular redox environment. DTT has a reduction potential of -330 mV at a pH of 7 while GSH/GSSG has a reduction potential of -264 mV at a pH of 7.4, which is more closely representative of a cellular environment (*Watson et al.,* 2002). A healthy cell has a reduction potential of -250 mV with a GSH to GSSG ratio of 100:1, while a damaged cell has a ratio of 1:100 of GSH to GSSG and a half cell potential of -170 mV (Figure 3) (*Schafer et al.,* 2001; *Watson et al.,* 2002). Therefore, GSH in its reduced form is representative of a healthy cell and as GSH is oxidized and converted to GSSG, it represents a damaged cell reaching apoptosis.

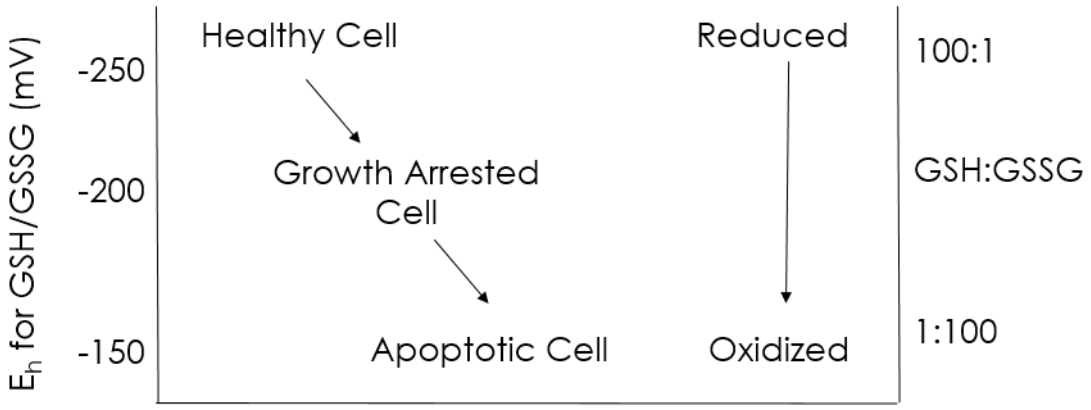

Figure 3. Cellular Damage indicated by the reduction potential and ratio of GSH to GSSG for a healthy cell, damaged cell, and apoptotic cell. (adapted from *Watson et al.*, 2002).

In the present study (i) a GSH method was optimized for determining oxidative capacity of PM and (ii) a number of CNP were characterized physico-chemically and tested with the GSH assay. By choosing a variety of soot particles with distinct morphologies, surface areas, particle sizes, trace metal and organic content, and microstructures the goal was to shed light on particle characteristics that drive particle toxicity based on oxidative potential. Results from this study will help scientists understand the detailed mechanisms or particle reactions and inform policy makers on what type of emissions are particularly harmful to public health. Toxicity of soot samples has been associated with their nanometer size, allowing them to reach far into the lungs and penetrate membranes, while providing an excess of surface area sites for reactions to occur at. Thus, determining surface area within the aqueous system and not in a dry environment is essential. This was achieved using a laser particle size analyzer. Further morphological and elemental characterization of particles were investigated with scanning electron microscope (SEM) and electron dispersive detection (EDS). Transition metals such as iron and copper are thought to act as catalysts in the reaction of soot with a nucleophile to produce ROS through Fenton chemistry. The Fenton reaction (Eqn. 6) describes the generation of ROS via the oxidation of Fe(II) by hydrogen peroxide (*Buda et al*., 2003).

$$Fe^{2+} + H_2O_2 \rightarrow Fe^{3+} + \bullet OH + OH^- \qquad \text{Eqn. 6}$$

Trace metal content was determined for CNP samples with inductively coupled plasma mass spectrometry (ICP-MS).

The majority of CNP material is made up of elemental carbon (EC) and organic carbon (OC), which are directly emitted through anthropogenic activities and generated in the atmosphere through gas-to-particle conversion in reaction with oxidative species. OC may contain polycyclic aromatic hydrocarbons (PAHs) and quinones (*Samara et al.*, 2014). EC is

derived directly from biomass and fossil fuel burning and is often used interchangeably with soot (*Long et al*., 2013). Here, we approximate OC in CNP samples by use of thermal gravimetric analysis (TGA), where samples are heated while recording the loss of mass over time. This gives an understanding of relative amounts of volatile OC and residual EC contents.

CHAPTER II

JOURNAL ARTICLE 1

“FLUOROMETRIC GLUTATHIONE ASSAY FOR PARTICULATE MATTER OXIDATIVE CAPACITY DETERMINATION”

CHAPTER II

FLUOROMETRIC GLUTATHIONE ASSAY FOR PARTICULATE MATTER OXIDATIVE CAPACITY DETERMINATION

ABSTRACT

Fine atmospheric particulate matter ($PM_{2.5}$) emitted during the combustion of fossil and biomass fuels is known to adversely affect human health. While the underlying mechanisms are thought to be driven by the generation of reactive oxygen species (ROS), specific particle characteristics responsible for this detrimental effect are not well understood. In this research, the quantitative determination of the biologically relevant antioxidant glutathione (GSH) was optimized for use as an indicator of particle oxidative capacity to shed light on relevant particle characteristics. This was accomplished by reacting GSH with the fluorescent marker *o*-phthalaldehyde (OPA) in phosphate buffered saline solution (PBS, pH 7.4). The signal detection and quantitation limits were determined to be 0.032 μM GSH and 0.49 μM GSH, respectively. Depletion of GSH followed first order kinetics during the 60-90 minute experiments with an average 4.2%$_{RSD}$. This allowed for the determination of pseudo first order rate constants that displayed high variability across samples with different physicochemical properties. This method provides an acellular assay to quantitate the oxidative capacity of particles in a biologically relevant medium, thus can be used to improve understanding of particulate toxicity.

INTRODUCTION

Anthropogenic activities associated with energy production such as transportation and home-heating are the main sources of fine ambient particulate matter ($PM_{2.5}$) that adversely affect respiratory and cardiovascular health as well as the environment and global climate (*Bell et al.,* 2009; *Bond et al.,* 2005; *Jacobson et al.,* 2010; *Niranjan et al*., 2017). Particle toxicity has been

associated with the generation of reactive oxygen species (ROS), which include the superoxide radical ($\cdot O_2^-$), hydrogen peroxide (H_2O_2), hydroperoxyl radical ($HO_2\cdot$), and hydroxyl radical ($\cdot OH$), whereby the production of these ROS seems to depend on specific particle characteristics, such as their small size, surface functional groups, as well as their organic, trace metal and elemental carbon contents (*Achilleos et al*., 2017; *Atkinson et al.,* 2015; *Brook et al.,* 2010; *Garcia-Fernandez et al.,* 2014; *Simkhovich et al.,* 2008). While much of this insight has been generated through expansive toxicity and epidemiological studies, there is a clear need for simple, acelluar assays that aid in determining a relative capacity of particle induced toxicity (*Grahame et al*., 2014; *Ristovski et al.,* 2012; *Xiong et al.,* 2017). The current most widely used such assay relies on the oxidation of dithiothreitol (DTT) and detection with UV-Vis spectrometry (*Cho et al.,* 2005; *McWhinney et al.,* 2013; *Charrier et al.,* 2012). Other assays have included the use of biological antioxidants, such as ascorbate (*Ayres et al.,* 2008; *Fang et al,* 2016). Here, we have optimized the fluorometric detection of glutathione (GSH), a thiol-containing tripeptide which plays a central role in the defense against cellular oxidative damage and in signaling pathways. A number of compelling reasons argue for its use to increase our understanding of the mechanisms that drive particle toxicity. First, GSH is a biologically relevant antioxidant that acts as a reducing agent partaking in the maintenance of cellular health such as converting peroxides to water (*Watson et al.,* 2002). GSH is present in the cellular system at average concentrations of 100 μM, which is significantly higher than that of other antioxidants such as ascorbate and nicotinamide adenine dinucleotide phosphate (NADPH); and absolute and relative concentrations of GSH and its oxidized glutathione disulfide (GSSG) are generally used to assess cell functionality and oxidative stress (*Hissin and Hilf,* 1976*; Schafer et al.,* 2001). By way of an example, at 100 μM total GSH concentration, a GSH:GSSG ratio of

100:1 is representative of a redox potential of -264 mV which is typical of a healthy cell. On the other hand, a GSH:GSSG ratio of 1:100 would have a redox potential of -150 mV as seen in an apoptotic cell (*Schafer et al.*, 2001; *Watson et al.*, 2002). For visualization, in Figure 4, the various redox pairs are arranged in increasing order of their reduction potentials relative to the standard hydrogen electrode (SHE) in pH 7 or 7.4 medium. DTT and NADPH, with reduction potentials of -330 mV and -400 mV, respectively, are positioned above the indicated cellular range, thus implying that even in a healthy cell, these two compounds would tend to be oxidized (*Watson et al.*, 2002; *W.W. Cleland*, 1964). In fact, NADPH effectively helps keep cellular GSH reduced (*Schafer et al., 2001*). Ascorbate on the other hand, with a reduction potential of -66 mV indicates that it remains reduced even in an apoptotic cell (*Borsook et al.*, 1933). Thus, to determine oxidative capacity of particles in the absence of the rest of the cellular system, reaction with GSH seems to be the most representative indicator. Finally, in terms of method sensitivity and specificity, fluorescence spectroscopy is more sensitive than the more regularly used UV-Vis

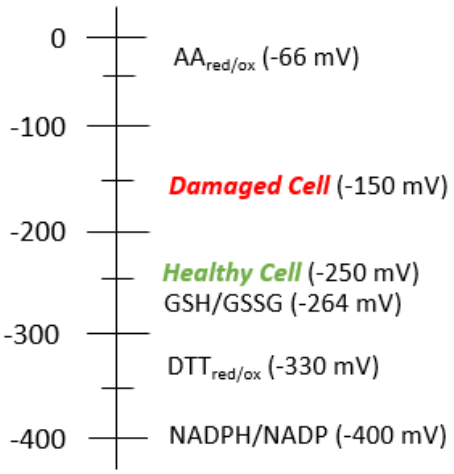

Figure 4. Standard Reduction Potentials relative to the standard hydrogen electrode (SHE) for redox pairs at a pH of 7 or 7.4.

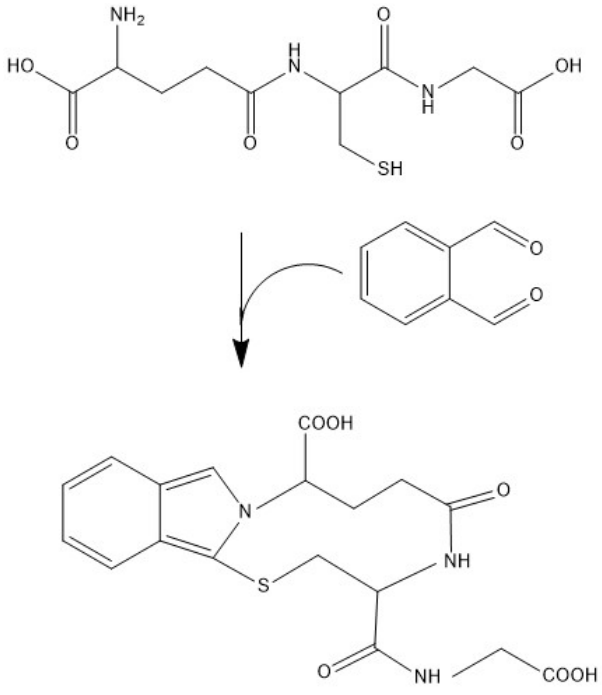

Figure 5. Reaction scheme of GSH reacting with OPA yielding a fluorescent GSH-OPA adduct that can be detected with an excitation of 340 nm and emission of 420 nm.

absorbance spectroscopy for the determination of some of the other antioxidants, including DTT; and the fluorescent reagent *o*-phthalaldehyde (OPA) is stable and works by binding in a 1:1 ratio specifically towards thiol amine pairs in that are in proximity, as shown in Figure 5 (*Hissin and Hilf*, 1976). After oxidation to GSSG, the binding site becomes unavailable for OPA, and therefore does not interfere with detection. While GSH analysis with this fluorescent marker is widely used by biochemists to asses and image redox potential within a cell, it has not been applied for the study of acellular particle oxidative properties as described here (*Hiroi et al.,* 2005; *Kandar et al.*, 2013; *Krzyżanowski et al.,* 2014). OPA has also been used in the determination of trace ammonium concentration in seawater by adding sulfite to the OPA reagent before reaction with the sample (*Hu et al*., 2014). Testing of the optimized method was performed on NIST Diesel PM, GfG, and XE2 soot samples as well as silica particles for a control.

EXPERIMENTAL SECTION

Reagents and Equipment

GSH was obtained as L-glutathione ≥ 98% from Sigma Aldrich and OPA from Tokyo Chemical Industry, Co. A 10.0 mM stock solution of GSH was prepared daily in 1x phosphate buffered saline solution (PBS) by diluting a pH 7.4 10x PBS stock buffer (55.34 g NaCl, 1.5 g KH_2PO_4, and 9 g Na_2HPO_4 in 500 mL 18.2 Megohm-cm water). A 1.0% (w/v) OPA solution was made daily by adding 0.10 g of OPA into 10.0 mL MeOH, resulting in a stock solution of 74.6 mM OPA. All experiments were carried out at room temperature within a few hours of solution preparation. Test particles consisted of NIST Diesel PM 2975 (NIST), Palas GfG (GfG), Printex XE2B (XE2), and SiO_2 (silica). The NIST sample was obtained from National Institute of Standards and Technology, XE2 from Orion, silica from Sigma-Aldrich (Silica Gel,

TCL high-purity grade without binder), and GfG was generated with a Palas GfG 1000 instrument through spark-discharge between two graphite rods under argon gas. XE2 and GfG are used as surrogate for soot particles and in conjunction with the NIST soot samples denoted as CNPs. Samples were filtered with 0.2 µm Watson™ Puradisc™ 25 mm syringe filters before analysis in a 1-cm quartz cuvette on the FluoroMax4 fluorometer from Jobin Yvon.

RESULTS AND DISCUSSION

Selection of Optimal Excitation and Emission Wavelengths and Reaction Time

The absorption spectrum of a 100.0 µM GSH (in 1x PBS) in Figure 6a shows that OPA bound to GSH has two close maxima at 340 and 355 nm that are absent in the OPA (in 1x PBS) reactant solution. Since the fluorescence emission signal maximum at 420 nm, as seen in Figure 6b,

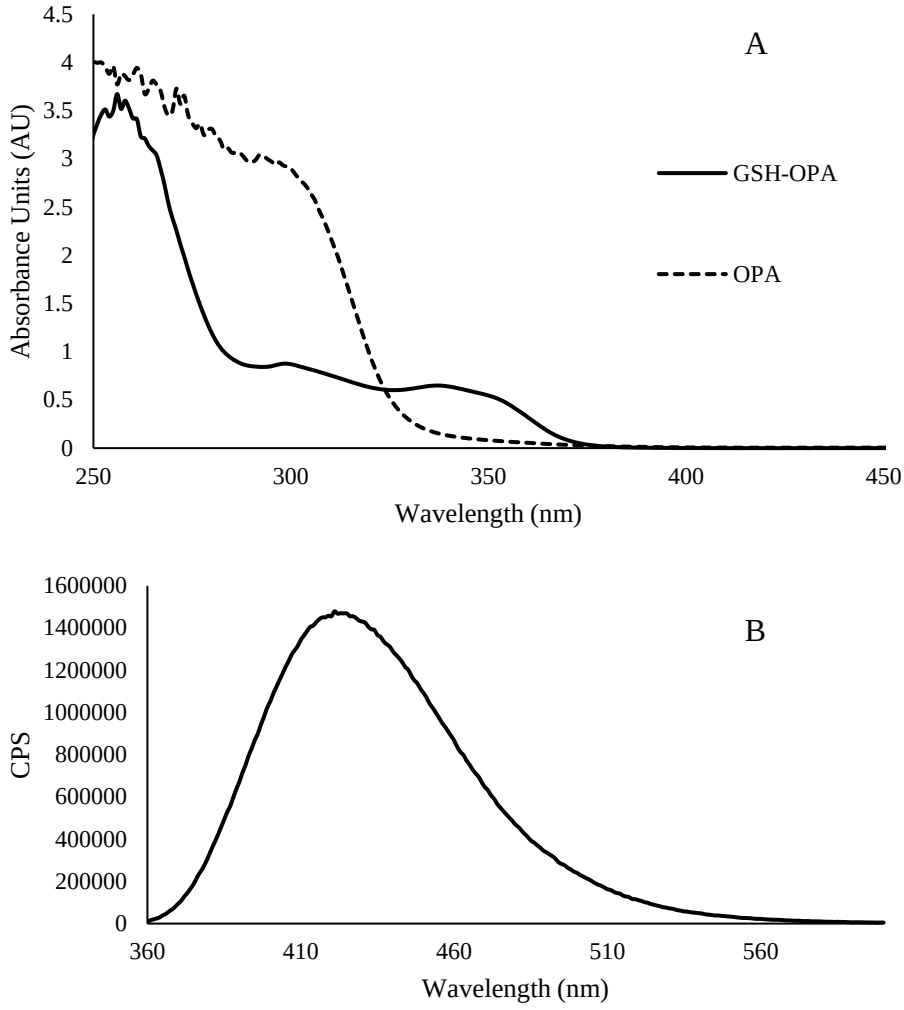

Figure 6. Detection of GSH-OPA by A) Absorbance spectrums of OPA (in 1x PBS) and GSH-OPA (in 1x PBS) determined via UV-Vis Spectroscopy. B) Emission spectrum of 100 µM GSH with 150 µL 1.0%(w/v) OPA following incubation of ten minutes at room temperature, determined by fluorescence spectroscopy with an excitation wavelength of 340 nm

was 4% higher using the excitation wavelength of 340 nm compared to 355 nm, 340 nm was chosen throughout the study (Figure 6b). These findings

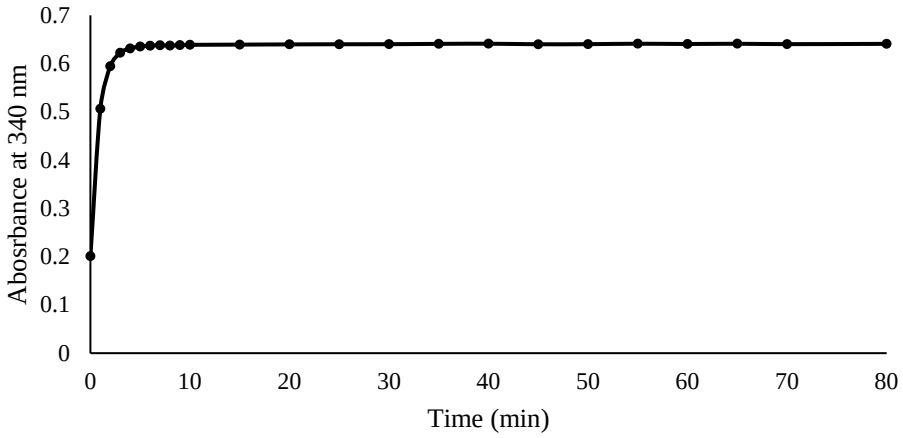

Figure 7. Reaction time of GSH-OPA adduct determined by UV-Vis spectroscopy with absorbance at 340 nm. Stability is reached after ten minutes and remains stable for the following seventy minutes.

are consistent with literature values (*Hissin and Hilf*, 1976; *Cohn and Lyle*, 1966; *Roušar et al.*, 2012). Timing of the reaction of OPA with GSH was studied via UV-Vis absorbance and is shown in Figure 7. Absorbance reached a maximum after ten minutes and remained stable throughout the end of the measurement period of 80 minutes. This stability in fluorescence signal of the GSH-OPA adduct lends itself useful for batch analyses.

Calibration Curve and Detection Limits

A representative calibration curve with standard solution concentrations of up to 100.0 µM GSH is shown in Figure 8. The relatively lower signal of the 250.0 µM GSH standard is due to secondary absorption and is thus not included in the calibration curve. Calibration standards vary

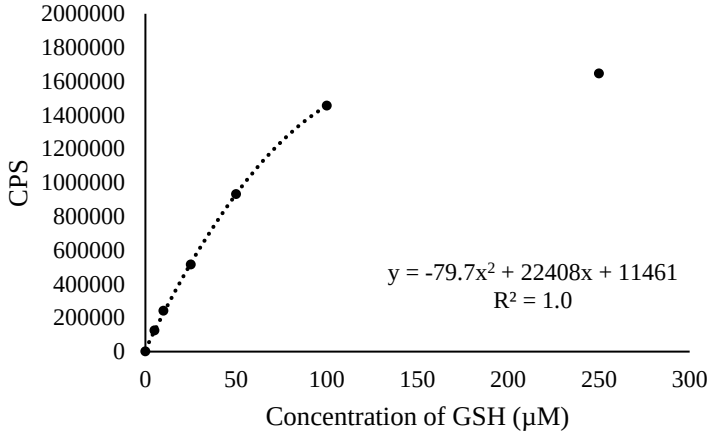

Figure 8. Calibration curve of GSH (0-100 µM) with OPA on the FluoroMax4. Secondary absorption is observed in higher concentrations (250 µM) and not included in the calibration curve. Calibration curves vary 4%$_{RSD}$ from day to day.

with an average relative standard deviation (RSD) of 4% RSD from day to day. Using standard techniques, the signal detection and quantitation limits were determined to be 0.032 and 0.49 µM GSH, respectively.

PM Oxidative Potential Experiment

To measure the oxidative potential of PM, the concentration of GSH was determined as a function of time in suspensions of 100 µg PM (mL 100.0 µM GSH)$^{-1}$. This was accomplished by adding 0.0120 g of PM and 3 drops of methanol to 118.8 mL of 1x PBS in an amber vial containing a stir rod. Before addition of 1.20 mL of 10.0 mM GSH (in 1x PBS), to make a final concentration of 100.0 µM GSH, the solution was sonicated for 2 minutes and then stirred on a stir plate on medium speed for 25 minutes. These parameters were determined and proved to ensure relatively stable particle dispersions for the duration of the experiment. An identically prepared control solution of GSH in 1x PBS without particles was run in parallel. Immediately after addition of GSH, and at set time intervals thereafter, a 3.0 mL aliquot was removed from the solution, pipetted directly into a syringe with a 0.2 µm Watson™ Puradisc™ 25 mm syringe filter tip and pushed through the filter directly into an amber vial containing 150.0 µL of 1.0%(w/v) OPA prepared in MeOH, resulting in a 3.7 mM OPA concentration. The vial was

capped, the solution was mixed through inversion and the sample was left to react for ten minutes before analysis on the fluorometer in a 1-cm quartz cuvette. Fluorescence photons in counts per second (CPS) were recorded at the emission wavelength of 420 nm and excitation at 340 nm, with slit widths set to 1 nm. CPS were converted to μm GSH using the calibration curve. Average concentrations of three replicate runs with one standard deviation error bars are shown in Figure 9 for the silica and three CNP samples. Respective single control runs are

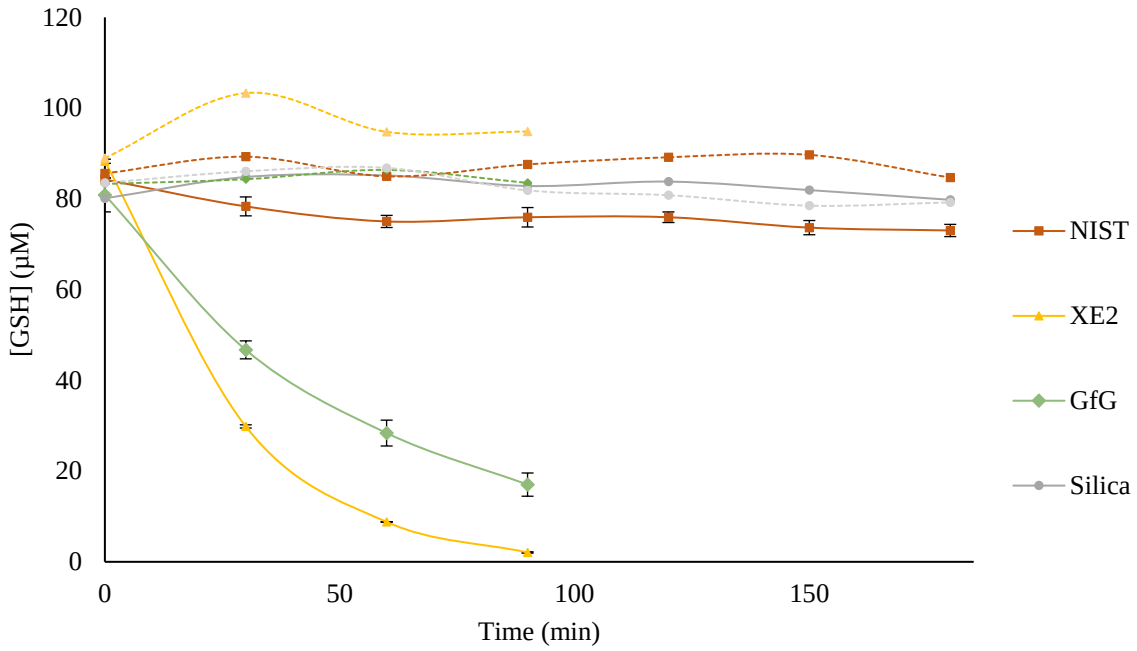

Figure 9. GSH exposed to untreated particles**.** Concentration of GSH over time of exposure to various samples (solid lines) as well as their respective controls (dashed lines). If error bars are not visible, it is due to the size of the data point symbol. Controls were only analyzed in one replicate for each sample.

shown in dashed lines. CNPs seemed to oxidize GSH to significantly varying degrees, with XE2 displaying the highest and NIST the lowest reactive. GSH concentrations in the silica control and the controls without particles remained essentially unchanged over the course of the 90-minute experiment.

Results show high reproducibility between replicate runs with an average RSD of 4.2%. Any potential interfering species that affect the OPA marker directly would stem from a soluble

ammonium and sulfite/thiol pair, with the one at the lowest concentration controlling the magnitude of enhanced fluorescent signal. Typical ammonium concentrations range from 1 to 10% by PM mass depending on size fraction and sampling location (*Tsai et al.*, 2012; *Yang et al.*, 2011). This would translate into a potential concentration of about 50-500 µM ammonium in this experimental setup. This would show as a false positive signal only in the co-presence of reduced sulfur (*Benson and Hare*, 1975). Since sulfite and thiols are absent from PM, this interference is unlikely in the current system (EPA, 2012).

A plot of ln[GSH] vs. time in for each of the CNPs reveal pseudo first order reactions with respect to GSH, forming linear relationships with R^2 values for CNP experiments ranging from 0.76 to 1.0 (Figure 10). The control does not exhibit first order decomposition, and has therefore been left out of the kinetics plot.

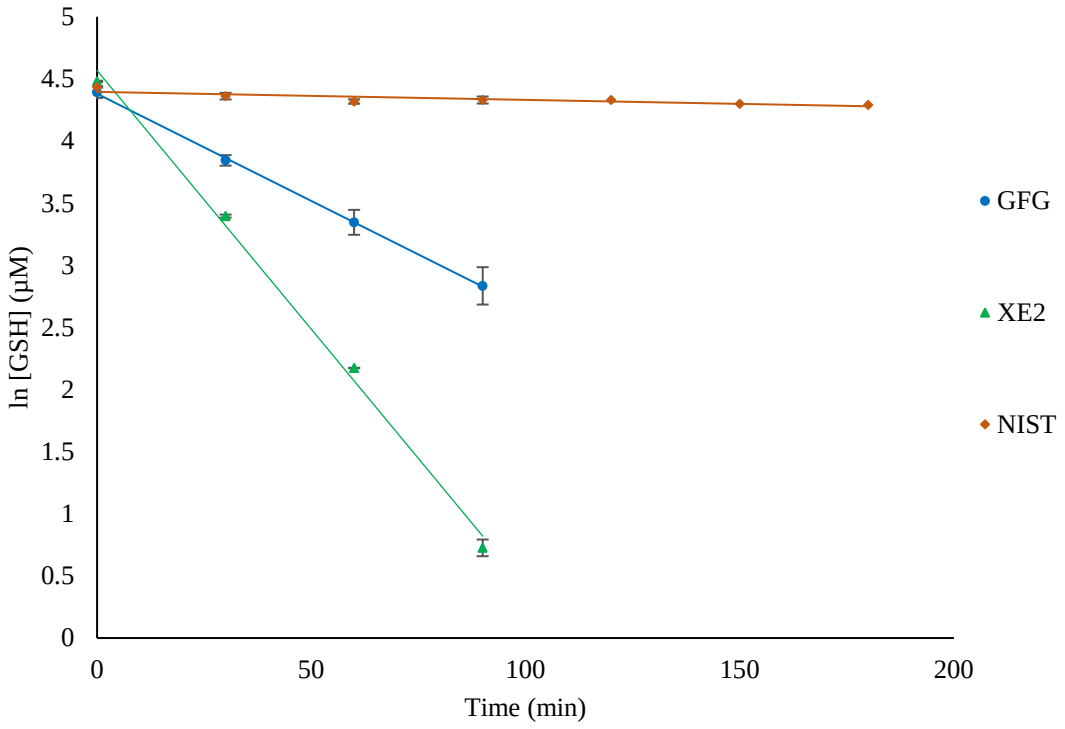

Figure 10. First order kinetics plots for GfG and XE2 reacting with GSH over a period of ninety minutes, displaying first order kinetics with respect to GSH.

The pseudo first order rate law indicates that the GSH oxidation occurs by first order mechnism(s) and that for the duration of the experiment there is an effective constant concentration of the oxidizing component in the CNPs (Eqn. 1).

$$\text{Rate} = k'[GSH]^1 \qquad \text{Eqn. 1}$$

Slower reacting PM (e.g. NIST) for which GSH was not consumed within 90-minutes continued to show first order reaction rates through the end of the 3-hour experiment.

This indicates that GSH is likely consumed in one oxidation process driven by PM rather than by two independent processes. Such as has been suggested for instance in reaction with a primary oxidant or a secondarily produced ROS (*Ayres et al.,* 2008). If the reaction were driven by secondarily produced ROS that depended on GSH as an electron donor, the reaction rate would not be first order. In addition, the pseudo first order reaction rate suggests that the carbonaceous matter component that leads to the oxidation of GSH remains constant throughout the experiment. This allows for the determination of a pseudo first order rate constant that is independent of GSH concentrations and that can be used for comparative purposes in the study of the reactivity of PM in the context of cellular toxicity. Pseudo first order rate constants (k'), were determined from the absolute value of the least squares fits of ln [GSH] vs. time. All replicate measurements were included for a given sample (Table 1). Half lives ($t_{1/2}$= ln 2/k') for GSH in the presence of the various black carbons and silica as well as in the controls are summarized in Table 1.

Table 1. Kinetic rate constants (k') and half-lives ($t_{1/2}$) for samples reacting with GSH (GfG, NIST, XE2) and their R^2 value for linear fit.

Sample ID	**k' (min^{-1})**	**S.D.**	**R^2**	**$t_{1/2}$ (hr)**	**S.D.**
GfG	0.0180	0.0008	1.0	0.64	0.03
XE2	0.0417	0.0009	1.0	0.277	0.006
NIST	0.0006	0.0001	0.76	18	3

CONCLUSION

A relatively simple fluorometric GSH assay was optimized for studying the oxidative potential of PM in PBS with an emphasis on CNPs, including diesel soot. The reaction of GSH with OPA is specific in this system, with signal detection and quantitation limits of 0.032 and 0.49 µM GSH, respectively. The dynamic calibration range extended to 100 µM GSH, which was the maximum GSH concentration added to PM slurries. Highly reproducible triplicate runs of all PM samples resulted in pseudo first order reaction rates with respect to GSH consumption with average relative standard deviations of 4.2%$_{RSD}$. This method provides a simple assay to gather robust complementary information that can help shed light on the particle characteristics that lead to the oxidation of the GSH, a key player in cellular health.

REFERENCES

(1) Achilleos, S.; Kioumourtzoglou, M. A.; Wu, C. Da; Schwartz, J. D.; Koutrakis, P.; Papatheodorou, S. I. *Environment International*. 2017.
(2) Atkinson, R. W.; Mills, I. C.; Walton, H. A.; Anderson, H. R. *J. Expo. Sci. Environ. Epidemiol.* **2015**.
(3) Ayres, J. G.; Borm, P.; Cassee, F. R.; Castranova, V.; Donaldson, K.; Ghio, A.; Harrison, R. M.; Hider, R.; Kelly, F.; Kooter, I. M.; Marano, F.; Maynard, R. L.; Mudway, I.; Nel, A.; Sioutas, C.; Smith, S.; Baeza-Squiban, A.; Cho, A.; Duggan, S.; Froines, J. In *Inhalation Toxicology*; 2008; pp 75–99.
(4) B. Z. Simkhovich, M. T. Kleinman, R. A. K. *J. Am. Coll. Cardinology* **2008**, *52* (9), 719–726.
(5) Bell, M. L.; Ebisu, K.; Peng, R. D.; Samet, J. M.; Dominici, F. *American Journal of Respiratory and Critical Care Medicine*. 2009, pp 1115–1120.
(6) Bond, T. C.; Sun, K. *Environ. Sci. Technol.* **2005**, *39* (16), 5921–5926.
(7) Borsook, H.; Keighley, G. *Proc. Natl. Acad. Sci. U. S. A.* **1933**, *19* (Vitamin C), 875–878.
(8) Brook, R. D.; Rajagopalan, S.; Pope, C. A.; Brook, J. R.; Bhatnagar, A.; Diez-Roux, A. V.; Holguin, F.; Hong, Y.; Luepker, R. V.; Mittleman, M. A.; Peters, A.; Siscovick, D.; Smith, S. C.; Whitsel, L.; Kaufman, J. D. *Circulation*. 2010.
(9) Charrier, J. G.; Anastasio, C. **2012**, 9321–9333.
(10) Cho, A.; Sioutas, C.; Miguel, A. H.; Kumagai, Y.; Schmita, D. A.; Singh, M.; Froines, J. R. *Environ. Res.* **2005**, *99*, 40–47.
(11) Cleland, W. W. *Biochemistry* **1964**, *4*, 480–482.
(12) Cohn, V. H.; Lyle, J. *Anal. Biochem.* **1966**, *14* (3), 434–440.
(13) EPA. *BC Emissions.pdf*; 2012.
(14) Fang, T.; Verma, V.; T Bates, J.; Abrams, J.; Klein, M.; Strickland, J. M.; Sarnat, E. S.; Chang, H. H.; Mulholland, A. J.; Tolbert, E. P.; Russell, G. A.; Weber, J. R. *Atmos. Chem. Phys.* **2016**, *16*, 3865–3879.
(15) Garcia-Fernandez, C.; Picaud, S.; Rayez, M. T.; Rayez, J. C.; Rubayo-Soneira, J. *J. Phys. Chem. A* **2014**, *118* (8), 1443–1450.
(16) Grahame, T. J.; Klemm, R.; Schlesinger, R. B. *J. Air Waste Manage. Assoc.* **2014**, *64*, 620–660.
(17) Hiroi, M.; Ogihara, T.; Hirano, K.; Hasegawa, M.; Morinobu, T.; Tamai, H.; Niki, E. *Free Radic. Biol. Med.* **2005**, *38*, 1057–1072.
(18) Hissin, P. J.; Hilf, R. *Anal. Biochem.* **1976**, *74* (1), 214–226.
(19) Hu, H.; Liang, Y.; Li, S.; Guo, Q.; Wu, C. *J. Anal. Methods Chem.* **2014**.
(20) Jacobson, M. Z. *J. Geophys. Res. Atmos.* **2010**, *115* (14).
(21) Kandar, R.; Vrbová, M.; Andová, J. Č. *J. Liq. Chromatogr. Relat. Technol.* **2013**, *36*, 2013–2028.
(22) Krzyżanowski, D.; Bartosz, G.; Grzelak, A. *Free Radic. Biol. Med.* **2014**, *76*, 47–52.
(23) McWhinney, R. D.; Badali, K.; Liggio, J.; Li, S.-M.; Abbatt, J. P. D. *Environ. Sci. Technol.* **2013**, *47* (7), 3362–3369.
(24) Niranjan, R.; Thakur, A. K. *Front. Immunol.* **2017**, *8* (JUN).
(25) Ristovski, Z. D.; Miljevic, B.; Surawski, N. C.; Morawska, L.; Fong, K. M.; Goh, F.; Yang, I. A. *Respirology*. 2012, pp 201–212.

(26) Roušar, T.; Kučera, O.; Lotková, H.; Červinková, Z. *Anal. Biochem.* **2012**, *423* (2), 236–240.
(27) Schafer, F.; Buettner, G. *Free Radic. Biol. Med.* **2001**, *30*, 1191–1212.
(28) Tsai, J.-H.; Lin, J.-H.; Yao, Y.-C.; Chiang, H.-L. *Aerosol Air Qual. Res.* **2012**, *12*, 263–274.
(29) W. H. Watson, Y. Chen, D. P. J. *Thiol Metab. Redox Regul. Cell. Funct.* **2003**, *17* (1–4), 328–331.
(30) Xiong, Q.; Yu, H.; Wang, R.; Wei, J.; Verma, V. *Environ. Sci. Technol.* **2017**.
(31) Yang, F.; Tan, J.; Zhao, Q.; Du, Z.; He, K.; Ma, Y.; Duan, F.; Chen, G.; Zhao, Q. *Atmos. Chem. Phys.* **2011**, *11*, 5207–5219.

CHAPTER III

JOURNAL ARTICLE 2

"OXIDATIVE CAPACITY AND PHYSICOCHEMICAL PROPERTIES OF SOOT PARTICLES"

CHAPTER III

OXIDATIVE CAPACITY AND PHYSICOCHEMICAL PROPERTIES OF SOOT PARTICLES

ABSTRACT

Carbon nanoparticles (CNP), a component of atmospheric fine particulate matter ($PM_{2.5}$) emitted during the combustion of fossil and biomass fuels are known to adversely affect human health. While mechanisms by which CNPs cause damage to cells are thought to be driven by the generation of reactive oxygen species (ROS), specific particle characteristics responsible for the detrimental effect are not well understood. In this research project, seven different CNPs, ranging from standard soot to graphene, were investigated in biologically relevant medium to shed light on chemical mechanisms that lead to depletion of the biologically relevant antioxidant, glutathione (GSH). Physicochemical properties of CNP particles were studied to determine morphology, surface area, particle diameter, trace metal concentration, and volatile organic carbon content. Results show that with the exception for one high-metal content CNP, particle reactivity did not correlate clearly with any one specific particle characteristic. However, heat treating CNPs up to 700 ^{o}C in $N_{2,}$ which removes volatile organic molecules, led to increased reactivity across the board. The exposed carbonaceous material is more reactive toward GSH oxidation, indicating inhibition of reactivity by volatile organic substances. These results have significant implications to describe what physical and chemical properties may drive particle toxicity.

INTRODUCTION

Carbon nanoparticles (CNP), a component of ambient fine particulate matter ($PM_{2.5}$) and in particular soot, consists of linked nanometer sized carbonaceous spheres that stem primarily from the incomplete combustion of organic matter such as fossil and biomass fuels. CNP has been associated with adverse health effects by affecting respiratory and cardiovascular systems; as well as with negative impacts on global climate by absorbing solar radiation, and influencing clouds, snow, and ice melt (*Bell et al.,* 2009; *Bond et al.,* 2005; *Jacobson et al.,* 2010; *Niranjan et al.,* 2017). CNP consist of a combination of elemental carbon (EC), organic carbon (OC), and various trace metals. EC, OC, and transition metals have been associated with the toxicity of soot particles. Polycyclic aromatic compounds (PAHs) have also been found to have a positive correlation with particle reactivity. However, in a number of studies, OC has also been found to have negative association with toxicity of particles in some studies (*Long et al.,* 2013; *Niranjan et al.,* 2017; *Rappazzo et al.,* 2015). Transition metals, iron and copper in particular, as well as quinones, including anthraquinone, are thought to act as catalysts in the production of reactive oxygen species (ROS) that cause oxidative stress and ultimately leads to cell death (*Faiola et al.,* 2011). ROS include superoxide radical ($\bullet O_2^-$), hydrogen peroxide (H_2O_2), hydroperoxyl radical ($HO_2\bullet$), and hydroxyl radical ($\bullet OH$). In addition, recent studies have shown that the EC content of PM may play a major role in the toxicity of soot particles (*Bell et al.,* 2009; *Cho et al.,* 2005; *Peng et al.,* 2009). The interaction of the various particle characteristics with cellular antioxidants and ROS remain elusive, however. Here we have chosen to utilize glutathione (GSH), a biologically relevant antioxidant to assess the oxidative potential of PM in a well-characterized system containing several different CNPs.

Seven different CNPs, with highly varying particle characteristics, were chosen to further our understanding of the mechanisms that control biological oxidative properties. These particles included one standard diesel soot, three manufactured carbon blacks (CB), one model soot generated in lab through spark discharge (GfG), and two EC endmembers, graphite and graphene. Samples were also heat-treated in N_2 atmosphere to further investigate the role of volatile organic carbon reactivity. Six different types of CNP containing model particles, and their heat-treated counterparts, were tested for oxidative GSH capacity. All particles were physicochemically characterized for aqueous surface area and morphology, total and soluble trace metal composition, and volatile organic carbon content.

Toxicity of soot samples has been associated with their nanometer size, allowing them to reach far into the lungs and penetrate membranes, and provide copious surface area for reactions to occur. Thus, determining particle size and surface area within the aqueous system, and not only in a dry environment, is essential. This was achieved using a laser particle size analyzer. Further morphological characterization of particles was performed with scanning electron microscope (SEM). In addition, elemental characterization was accomplished with electron dispersive detection (EDS) and inductively coupled plasma mass spectrometry (ICP-MS). Elemental characterization is important because transition metals such as iron and copper are thought to act as catalysts in the reaction of soot with a nucleophile to produce ROS through Fenton chemistry. The Fenton reaction (Eqn. 7) describes the generation of ROS via the oxidation of Fe(II) by hydrogen peroxide (*Buda et al.*, 2003).

$$Fe^{2+}_{(aq)} + H_2O_{2\,(aq)} \rightarrow Fe^{3+}_{\ (aq)} + \bullet OH_{\ (aq)} + OH^-_{\ (aq)} \qquad \text{Eqn. 7}$$

OC may contain PAHs and quinones (*Samara et al.*, 2014). EC is derived directly from biomass and fossil fuel burning and is often used interchangeably with soot (*Long et al.*, 2013).

The bulk material of CNPs is made up of elemental carbon (EC) and organic carbon (OC), both of which have been implicated in particle toxicity, EC by providing electrons to O_2, forming ROS, and OC due to toxic PAHs and quinones. Here, we qualitatively determine OC in CNP samples by use of thermal gravimetric analysis (TGA), where samples are heated while recording the loss of mass over time. This gives an understanding of relative amounts of volatile OC and residual EC contents.

In this study, physicochemical properties of a variety of CNP are investigated and correlated with the oxidative capacity of CNP toward GSH to shed light on the detailed mechanisms behind particle toxicity.

MATERIALS AND METHODS

Particulate Matter (PM)

PM consisted mainly of CNPs, including NIST Diesel PM 2975 (NIST), Palas GfG (GfG), Printex XE2B (XE2), Flammruss 101 (F101), Printex 90 (P90), graphite (GRI), and graphene (GRE). SiO_2 (silica) was used as a control. The NIST Diesel PM sample was obtained from the National Institute of Standards and Technology (NIST); XE2, P90 and F101 from Orion; and graphite and graphene from Alfa Aesar. Silica was from Sigma-Aldrich (Silica Gel, TCL high-purity grade without binder). GfG was generated with a Palas GfG 1000 instrument through spark-discharge between two graphite rods under argon gas. XE2, P90, GfG, and F101 act as surrogates for soot particles. Graphite and graphene are included as end points for structure and purity.

Particle Oxidative Potential

The oxidative capacity of particles was determined by way of the oxidation of GSH following procedures in *Troth and Johansen* (2018). In brief, PM slurries of 100 µg per mL of phosphate buffered saline (PBS, pH 7.4) were spiked with 10 mM GSH in PBS to make a final concentration of 100 µM GSH. After inversion, a 3-mL aliquot of solution was immediately extracted by pipette and filtered with 0.2 µm Watson™ Puradisc™ 25 mm syringe filters, then reacted with 150 µL 1.0%(w/v) *o*-phthalaldehyde (OPA) for at least ten minutes at room temperature before analysis in a 1-cm quartz cuvette on a fluorometer (Jobin Yvon FluoroMax4). The excitation wavelength was 340 nm and the emission wavelength was 420 nm with slit widths of 1 nm. Collection and analysis of sample aliquots was then repeated at set time intervals for a total of up to three hours. Samples were analyzed both untreated and after heat-treating at 700 °C in a furnace (MTI OTF-1200x) under N_2 gas. All experiments were performed in triplicate alongside a GSH control in the absence of CNP. Psuedo first order rate constants (k') were used to determine the half-life ($t_{1/2} = \ln 2/k$) of GSH in the presence of CNP (*Troth and Johansen,* 2018).

Aqueous Surface Area

The surface area of particles during reaction with GSH was determined with a laser particle size analyzer (Malvern Mastersizer 3000). The reaction was carried out analogous to the fluorometric GSH assay with particles in PBS and GSH spiked in to a final concentration of 100 µM. It was established that sonication of the CNP and PBS slurry for two minutes followed by stirring for 25 minutes resulted in relatively stable suspensions for the duration of the

experiments. Average surface areas and standard deviations throughout the experimental time frame were recorded and provide an estimate of variate in surface area.

Morphology and Elemental Analysis

CNP samples were imaged on a scanning electron microscope (SEM, FEI Quanta FEG 250) to observe their morphologies. Untreated samples were imaged using concentric backscatter (CBS) and secondary electron hybrid imaging. Heat-treated samples were imaged using secondary electron imaging. The accelerating voltage was 5.0 kV. Samples were analyzed with an energy-dispersive (EDS) detector on the SEM for elemental analysis with an accelerating voltage of 20.0 kV.

Trace Metal Content

Total and soluble trace metal content of CNP samples were determined with ICP-MS (Agilent 8900 ICP-QQQ). Digestion was performed with 0.10 mg mL^{-1} of each CNP sample in a solution of 75% acetone and 25% 1 N nitric acid following procedures in *Herner et al*. (2006). For soluble trace metals, samples were leached as in the oxidative potential determination methods, filtered, and acidified to 1% HNO_3 before analysis on ICP-MS.

Volatile Organic Carbon Content

Investigation of volatile organic carbon content was completed by thermal gravimetric analysis (TGA, Netzsch STA 449 F5). Samples were heated under N_2 with a ramping rate of 5 ˚C/min up to 850 ˚C, then held at a constant temperature for 20-minutes, followed by the temperature ramped down at 5 ˚C/min.

Graphene and Carbon Microstructure

The graphite-like microstructure and their defects were studied via Raman microspectroscopy (ReniShaw InVia Raman Microscope). Samples were analyzed following methods published elsewhere (*Ess et al.,* 2016; *Ferreria et al.,* 2010; *Gaffney et al.,* 2015; *Sadezky et al.,* 2005). The instrument was equipped with a Leica DMIRBE inverted optical microscope and a charge couple device (CCD) detector. In brief, samples were analyzed with a laser excitation source at 514 nm at approximately 0.1 mW through a 50x Leica inverted optical microscope and the Raman scattered light from the sample was collected by the same objective and analyzed through the inVia Spectrometer, and focused on a CCD camera.

RESULTS AND DISCUSSION

Oxidative Capacity of Particles

Oxidative capacity as determined with the GSH assay show that reactivity was greatest for untreated XE2, P90, and graphene (GRE), while graphite (GRI) was the least reactive (Figure 11a). Heat-treatment of samples (700 ºC, N_2) generally increased reactivity toward GSH, frequently consuming nearly all of the antioxidant in 60-minutes (Figure 11b), in particular for the soot generated from a diesel forklift (NIST).

Evaluation of the kinetics of the reaction of CNP with GSH revealed first order reaction rates with regard to GSH, as seen by the linear least-squares-fits of ln[GSH] vs. time plots in Figure 12 (Eqn. 8). Pseudo first order reaction rate constants (k', min^{-1}) and standard deviations were determined for each sample from the slopes through all replicate measures.

$$\text{Rate} = k'[GSH] \qquad \text{Eqn. 8}$$

The pseudo first order rate constants with their standard deviations and R^2 values for the linear regression lines are summarized in Table 2. Generally, R^2 values range from 0.62 to 1.0 for untreated CNPs and 0.69 to 0.99 for heat-treated CNPs. Exceptions are untreated F101 with an

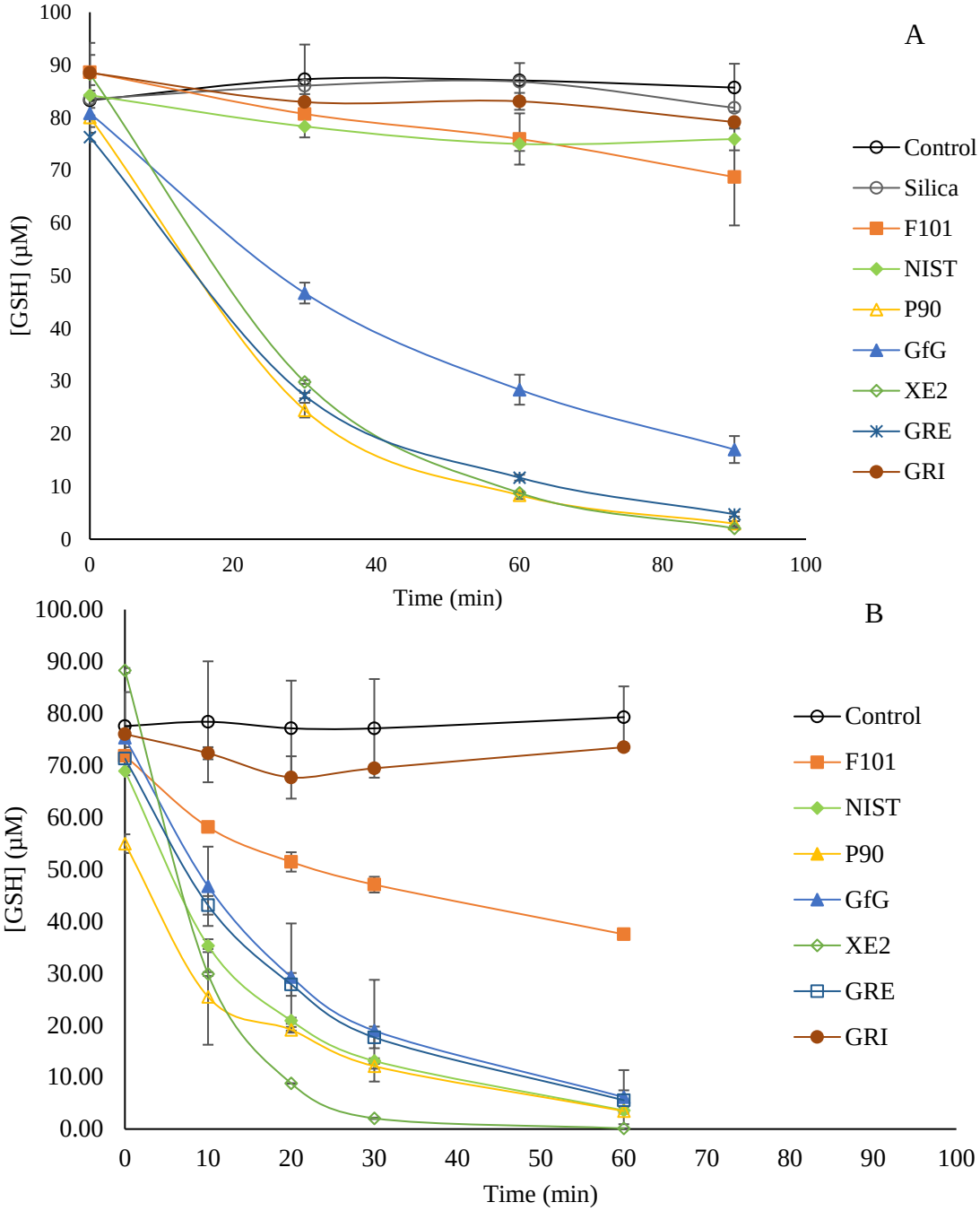

Figure 11. GSH exposed to (A) untreated particles and (B) heat-treated particles for 90 and 60-minutes. Error bars that are not visible are hidden due to the size of the data point symbol, with the exception of the silica sample, which only had one trial. The control is averaged from all untreated trials (N=8).

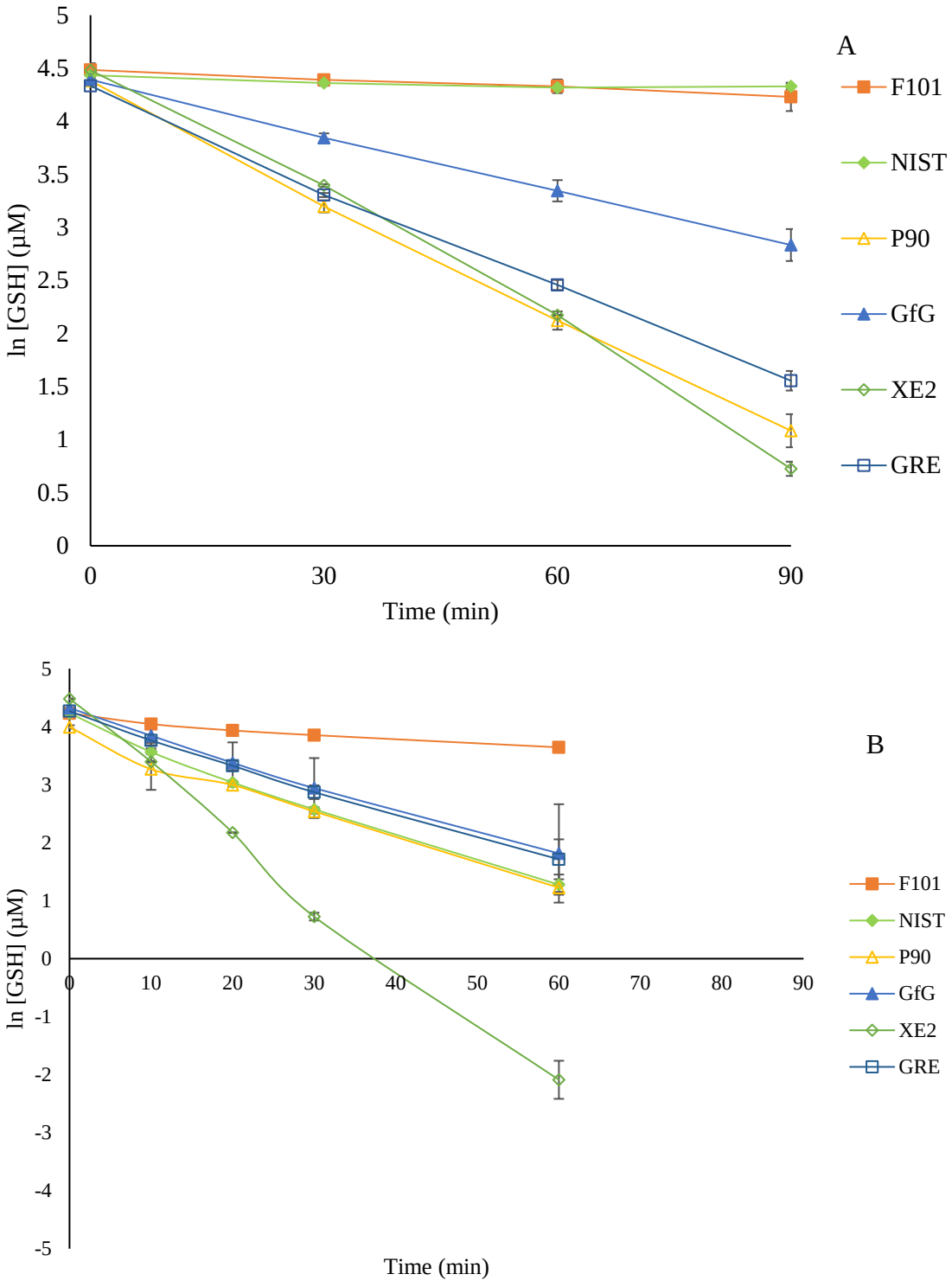

Figure 12. First order kinetics plots for (A) untreated and (B) heat-treated particles in the reaction with GSH. *R^2 value for GRI indicates forced first order fit.

R^2 value of 0.43, and heat-treated graphite with an R^2 value of 0.01. GSH consumption by a first order reaction is indicative of (i) a surplus of active sites on the CNP surfaces and (ii) the

presence of one reaction mechanism (*Troth and Johansen*, 2018). The control and silica, and graphite samples showed zeroth order kinetics with no significant change in GSH concentration over time, however for comparative purposes, a first order fit was forced to the graphite data to retain information about its slow reactivity. An R^2 value of 0.01 indicates the poor fit, however, calculation of k' and its standard deviation resulted in a k' value of 0.00102 with %RSD equal to 8.8% for untreated graphite.

Table 2. Pseudo first order rate constants and half-lives for GSH oxidation in the presence of PM.

						Heat-treated				
Sample ID	**k' (min^{-1})**	**S.D.**	**R^2**	**$t_{1/2}$ (hr)**	**S.D.**	**k' (min^{-1})**	**S.D.**	**R^2**	**$t_{1/2}$ (hr)**	**S.D.**
F101	0.0025	0.0007	0.43	5	1	0.0102	0.0008	0.93	1.13	0.09
NIST	0.0006	0.0001	0.62	18	3	0.048	0.002	0.99	0.238	0.008
P90	0.037	0.001	0.99	0.315	0.008	0.044	0.003	0.93	0.27	0.02
GfG	0.0180	0.0008	0.97	0.64	0.03	0.05	0.01	0.69	0.21	0.04
XE2	0.0417	0.0009	1.0	0.277	0.006	0.061	0.006	0.87	0.19	0.02
GRE	0.0174	0.0009	0.97	0.67	0.03	0.043	0.002	0.97	0.27	0.01
GRI*	0.00102	0.00009	0.88	11	1	0.0002	0.0007	0.01	48	142

*GRI did not follow first order kinetics, but was calculated in this way for comparison, causing a large S.D.

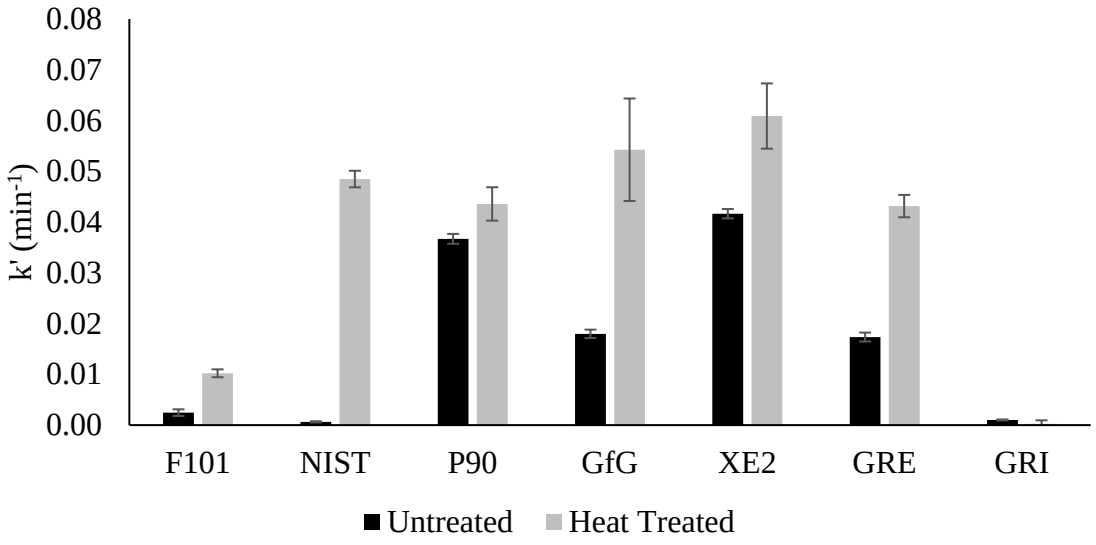

Figure 13. Rate constants for untreated and heat-treated particles from pseudo first order consumption of GSH.

Half-lives were determined by $t_{1/2} = \ln 2/k'$ and are listed in Table 2. For visualization of the impact of heat-treatment on particle reactivity, pseudo first order rate constants for all samples are graphed in Figure 13. The magnitude of k' varies across samples with varying physical and chemical properties and significant difference is observed between rate constants for untreated samples and their heat-treated counterparts, with the exception of graphite.

Table 3. Specific surface areas of samples during their reaction with GSH for 50-minutes, determined on the Malvern Mastersizer 3000.

Sample ID	Specific Surface Area (m^2/kg)	S.D.
F101	9×10^2	5×10^2
NIST	5.9×10^2	0.2×10^2
P90	2.6×10^2	0.1×10^2
GfG	2.0×10^3	0.7×10^2
XE2	6×10^3	1×10^2
GRE	7×10^2	2×10^2
GRI	3×10^2	1×10^2
Silica	7.3×10^2	N/A

Surface Area and Morphology

Surface areas of CNP samples in GSH containing PBS were determined under analogous conditions as in the fluorometer GSH assay. Average specific aqueous surface area and standard deviations for each sample are listed in Table 3 and shows significant variation. Standard deviations of surface areas are representative of the change over a 50-minute time period. This variation does not seem to affect particle reactivity towards GSH, however, as the surface area over time during the reaction between CNPs and GSH was not found to correlate with k' values, indicating that surface area does not play a major role in these experiments.

Morphologies were qualitatively compared through SEM imaging for each CNP both before and after heat treatment (Appendix A). Some samples are distinct while some have similar features. For instance, all combustion-derived particles, i.e. F101, XE2, NIST, and P90 appear as spherical linked aggregates. The relative diameter of spheres decrease in size from F101 having approximately 350-450 nm to approximately 50 nm in the order listed. Gfg appears as large chunks of graphite, which may be due to the production by spark between two graphite

rods. Graphite is unique in that the particles are composed of sheets of graphite with a variety of lengths from 1 to 5 nm with rigid edges. Graphene appears as a disarray of sheets ≤1 nm in size. Heat treatment does not seem to result in visible morphological changes. Images for untreated and heat-treated samples may appear slightly varied as they were analyzed in two separate batches with two different imaging techniques at distinct magnifications.

Trace Metal Content

Trace metals such as iron, copper, and manganese can act as catalysts in redox reactions of PM with antioxidants (*Brook et al.*, 2010). For this reason, total and soluble trace metal content of the CNP particles was determined via acid digestion and leachates in PBS, respectively. The determination of total trace metals by ICP-MS acid digestion agreed with elemental analysis completed on the SEM with the EDS detector (Appendix B). XE2 is a

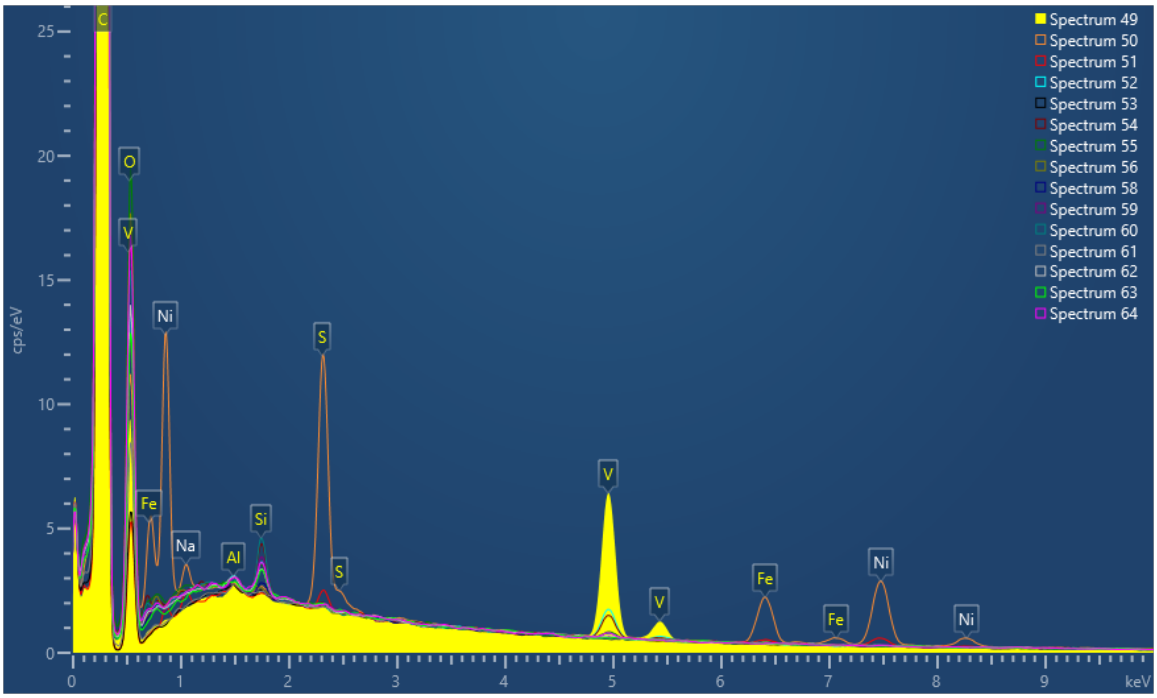

Figure 14. Overlaid EDS spectra for XE2 at a decreased maximum y-axis for comparison of all elements excluding carbon, whereas carbon generates a large peak as it is in the most abundance of the sample.

conductive CNP to which metals are intentionally added. XE2 was found to have vanadium, iron, sulfur, iron, and nickel by elemental analysis, which agreed with ICP-MS acid digestion data (Figure 14). Vanadium is produced from a source of heavy fuel combustion. Relative amounts of elements in CNP samples can be determined by the obtained EDS spectra, where it is clear there is a large abundance of carbon, also containing other trace elements.

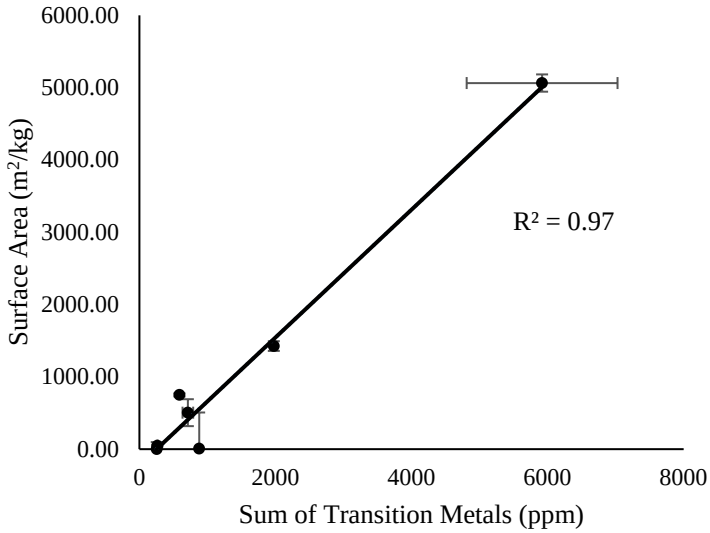

Figure 15. Sum of Total Trace Metals vs Surface Area. Transition metals Ti-Zn were included in the sum of the trace metals as they may participate in redox activity.

In terms of soluble trace metals, a significant portion, e.g. 50% for Fe, comes from the background itself. For total metals analyzed via strong acid digestion, Figure 15 shows a positive correlation between transition metal content (Ti through Zn) and the surface area of particles. This indicates that trace metals are adsorbed to the surface of the CNP particles, where they may be able to participate in redox cycling, and thus affect GSH oxidation.

Volatile Organic Carbon Content

Thermal gravimetric analysis (TGA) was carried out to study the mass lost from CNP while being heated to 850 ºC under N_2 in order to characterize the contribution of volatile organic molecules. Profiles in Figure 16 show the mass percent of samples as they are heated. Samples have unique profiles, where some show a gradual, near-linear decrease in mass and others display sudden decreases in mass percent, in particular at 600 ºC. Temperature profiles are

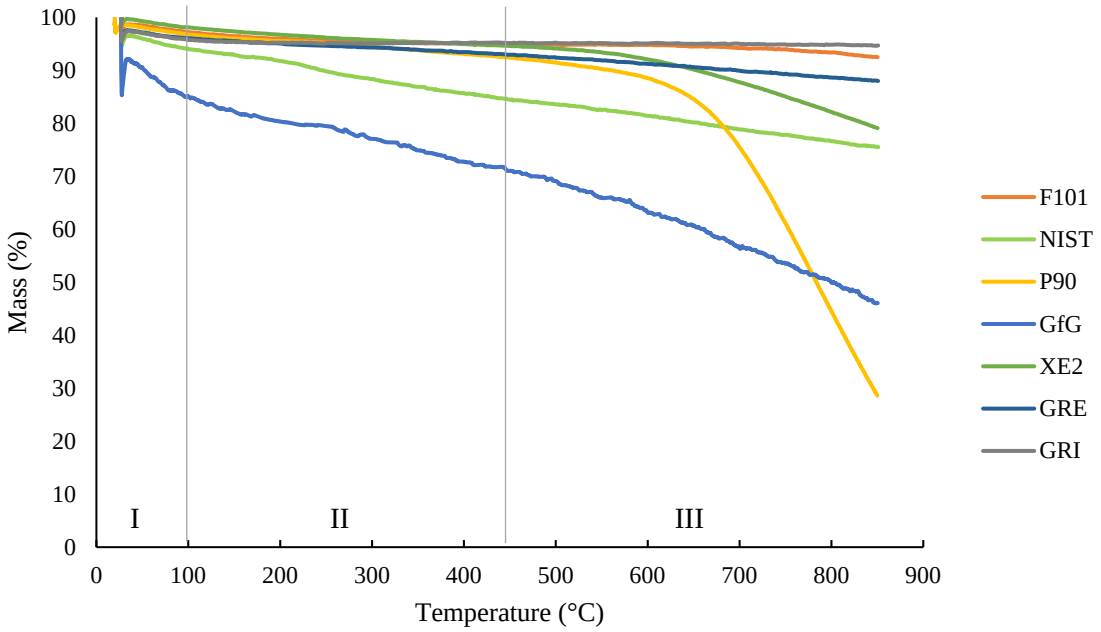

Figure 16. Mass percent of CNP samples as the temperature increases to 850 °C.

partitioned into three phases following standard protocol (*Bredin et al.*, 2011). In phase I, from 0-100 ºC, highly volatile molecules, including H_2O and low molecular weight organic compounds, are evaporated from CNP samples. Phase II ranges from 100-450 ºC, where medium volatile molecules are lost. These may include organic molecules such hydro/polycyclic aromatic hydrocarbons (PAHs), and their respective quinones, which have been tied to the reactivity of PM and soot (*Antiñolo et al.*, 2015). Average PAH boiling points are around 340 ºC, with anthroquinone evaporates at 380 ºC, naphthalene, anthracene, and benz(a)anthracene at 218 ºC, 340 ºC, and 438 ºC, respectively. Phase III includes the remaining range up to 850 ºC. Possible higher molecular weight molecules could

Table 4. Mass loss (Δm) of CNP at increasing temperatures, where 100-25 C represents Phase I, 450-100 C represents Phase II, and 700-450 C represents phase III.

	Mass Loss (Δm, ºC)		
Sample ID	**100-25**	**450-100**	**700-450**
F101	2.8%	2.3%	3.4%
NIST	6.0%	9.6%	11 %
P90	3.3%	4.4%	20%
GfG	15%	14 %	30%
XE2	1.9%	3.5%	8.8%
GRE	3.9%	3.1%	7.0%
GRI	4.3%	0.58%	4.4%

evaporate early in this range, such as benzopyrene, which evaporates at 495 ºC. At higher temperatures, such as 700 ºC, pyrolysis of soot is expected (*Bredin et al.*, 2011).

Plotting the loss of mass (Δm) for each sample at 100, 450, and 700 ºC gives insight into the chemical composition of these samples (Figure 18). It can be seen that the blue sector of each line shows relative amounts of highly volatile molecules, where GfG has the greatest amount of material lost in only this region compared to other samples. Next, NIST has the largest component of low and medium volatile substances. This is significant as NIST reactivity increases the most significantly following heat treatment. The impact of PAHs on PM toxicity has been thought to enhance particle reactivity; however, recent studies are finding that PAHs are not significant, and that rather elemental carbon (EC) correlates with particle toxicity (*Bell et al.*, 2009; *Cho et al.*, 2005; *Peng et al.*, 2009). Our data supports these findings, as seen in Figure 17. There is a correlation between the change in pseudo first order rate constant after heat treatment and the loss of PAHs (Phase II mass loss).

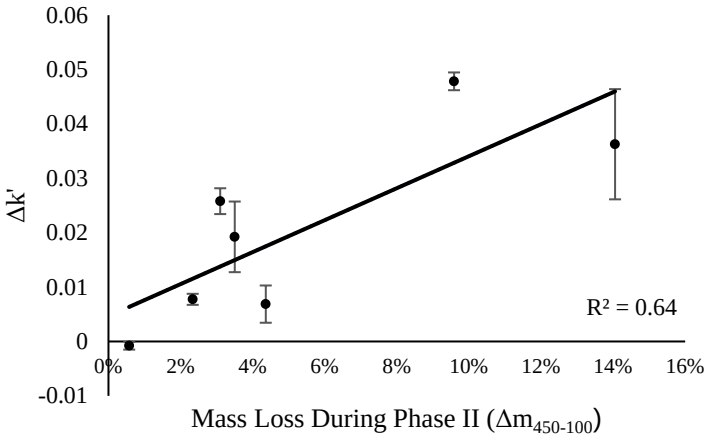

Figure 17. Correlation between mass loss during Phase II and the change in rate constant, k', after heat treatment.

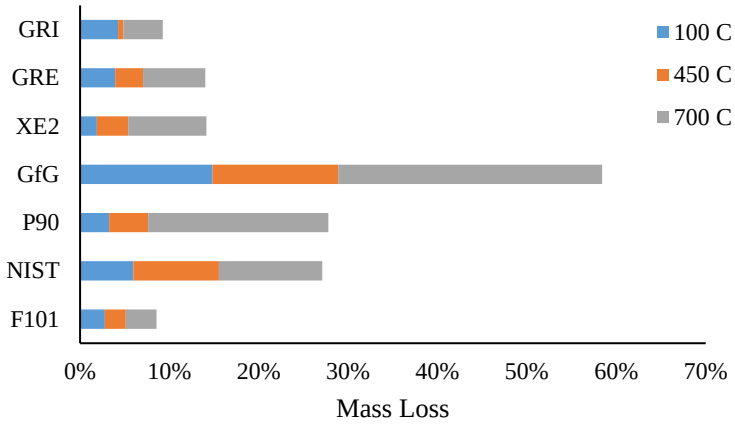

Figure 18. CNP mass loss at increasing temperatures.

Heat treatment of samples may also alter the microstructure and hybridization of C-C bonding, increasing elemental carbon-like structure with sp^2 hybridization. Graphene has been shown to have high transport of electrons due to sp^2 hybridization and arrangement of monolayers (*Ferreira et al.*, 2010). This would allow for the transfer of electrons in a redox reaction to occur with less energy required, making it a more favorable reaction, and would explain the observed increase in reactivity for CNPs. The EC component may be a driving force behind the toxicity of CNP particles to be investigated. Hybridization of carbon-carbon bonds have potential to influence the reactivity of particles and can be investigated by Raman microspectroscopy (*Müller and Schögl*, 2006).

Multilinear regression analysis was performed on the data set and found no significant correlation between transition metals and reactivity, or surface area and reactivity, but surface area and transition metals did have a correlation, as is supported by Figure 15. Fe and Cu are the transition metals that are most likely to participate in redox reactions through Fenton chemistry, but were not found to have a direct correlation between the sum of Fe and Cu in samples and their respective rate constants. While this does not eliminate the possibility of transition metals assisting in redox reactions, it cannot be proven as the driving force behind particle toxicity or oxidative capacity. When performing multilinear regression analysis, it was found that the pseudo first order rate constant, k', for heat-treated samples could be modeled with the mass loss after being heated to 700 $^{\circ}$C and the sum of transition metals (Ti-Zn) as co-variables. This model had an R^2 value of 0.708. After standardizing the coefficients for these two variables, it was determined that both the sum of transition metals and the mass lost after being heat-treated has approximately equal contribution to the rate constant (Table 5). Other models were tested and sensitivity testing was performed. The model in Table 5 and Figure 19 describe the given data set

best with the largest R^2 value, and smallest constant. Having a large constant indicates that the model is missing a parameter to describe the data set. Therefore, optimizing for the largest R^2 and smallest constant provides the most accurate model.

Table 5. Correlation for multilinear regression analysis model describing k' for heat-treated samples.

	Unstandardized Coefficients		Standardized Coefficients	t	Sig.	95.0% Confidence Interval for B	
	B	Std. Error	Beta			Lower Bound	Upper Bound
(Constant)	0.012386	0.010303		1.202154	0.295603	-0.01622	0.040992
700 C	0.09533	0.045396	0.568214	2.099969	0.103657	-0.03071	0.22137
Transition Metals	7.36E-06	3.41E-06	0.583863	2.157802	0.097128	-2.1E-06	1.68E-05

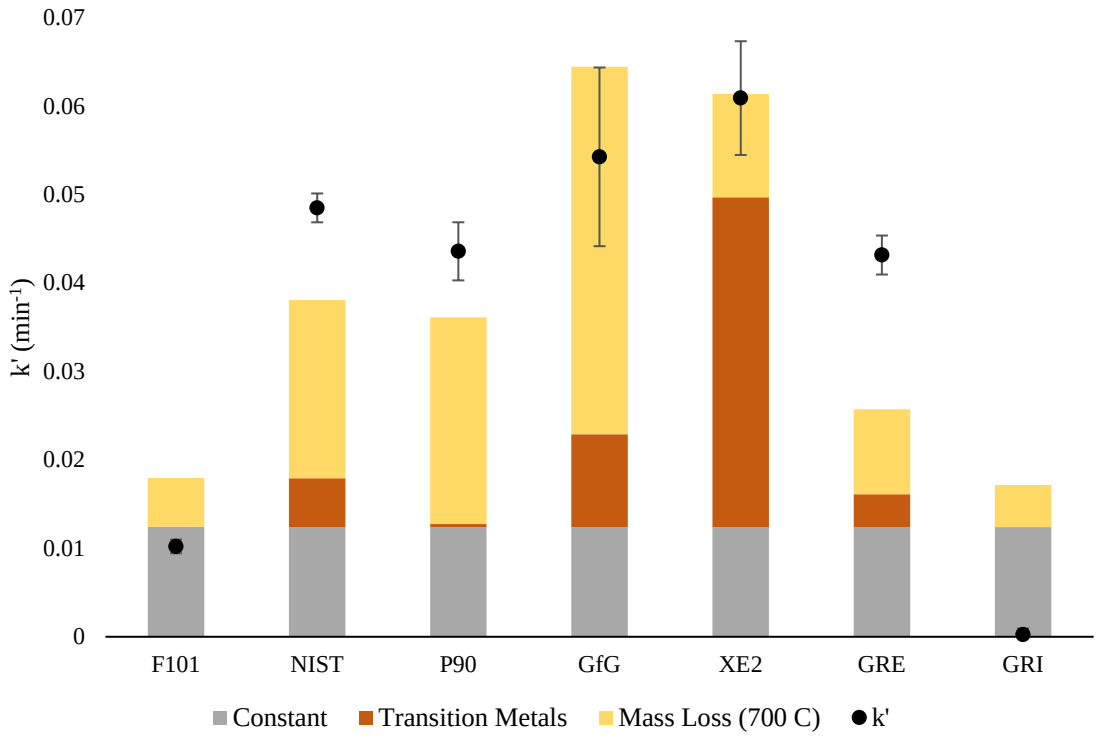

Figure 19. Calculated k' versus experimental k' for heat-treated samples.

The standardized coefficients and constant create an equation to predict values (Eqn. 9).

$$k'_{H,calc} = 0.09533\,[\Delta m_{700\text{-}450}] + 7.36\times10^{-6}\,[\text{Transition Metals (Ti-Zn)}] + 0.0123 \quad \text{Eqn. 9}$$

Calculated $k'_{H,calc}$ values can be compared to experimental k'_{H} values in Figure 19, where the components determined by the model are represented in stacked lines, summing up to $k'_{H,calc}$. The experimental k' values and their standard deviations are represented by black symbols. It can be observed the graphite is not well represented by this model, as it is the only sample that had a decrease in its rate constant. However, when graphite is removed, the R^2 value of the model decreases. The constant (gray) is high and is affecting the representation of samples, indicating that another variable needs to be considered. The appropriate variable to include in the model is likely the elemental carbon (EC) component, and could change the discrepancy in graphene's calculated versus experimental pseudo first order rate constants as well as the underestimation of graphene and NIST samples.

CONCLUSION

Oxidative capacity for one standard diesel sample and six other surrogate CNP samples was determined by GSH consumption and showed that soot with varying physicochemical properties have unique oxidative potentials, as described by their pseudo first order rate constants. Physical and chemical properties were correlated with rate constants for consumption of GSH by CNP. Surface area correlated with the pseudo first order rate constant for untreated samples with an R^2 value of 0.622, but after removal of sample XE2 from the correlation plot, it was found there is no correlation between surface area and k'. It was found that trace metals may play a significant role when present at high concentrations, and that midsize organic molecules with boiling points up to 450 ˚C may be inhibiting PM reactivity. The combination of these

physical and chemical properties may be responsible for overall reactivity, as was described by the multilinear analysis regression model. EC and its structure seems to be the driving force behind particle toxicity. This is to be further investigated and correlated with the current data set in future work.

Future work will further investigate the role of iron and copper in particle toxicity toward the biologically relevant antioxidant, GSH. Detection of ROS species may also be investigated as further proof of an oxidation pathway for consumption of GSH by CNP. Investigation of CNP samples by Raman microspectroscopy before and after heat-treatment will be completed in future work to determine the change in microstructure and correlation between the EC component and pseudo first order rate constants.

REFERENCES

(1) Antiñolo, M.; Willis, M. D.; Zhou, S.; Abbatt, J. P. D. *Nat. Commun.* **2015**, *6*, 6812.
(2) Bell, M. L.; Ebisu, K.; Peng, R. D.; Samet, J. M.; Dominici, F. *American Journal of Respiratory and Critical Care Medicine*. 2009, pp 1115–1120.
(3) Benson, J. R.; Hare, P. E. *Proc. Natl. Acad. Sci.* **1975**, *72* (2), 619–622.
(4) Bond, T. C.; Sun, K. *Environ. Sci. Technol.* **2005**, *39* (16), 5921–5926.
(5) Bredin, A.; Larcher, A.; Mullins, B. *Tribol. Int.* **2011**, *44* (12), 1642–1650.
(6) Brook, R. D.; Rajagopalan, S.; Pope, C. A.; Brook, J. R.; Bhatnagar, A.; Diez-Roux, A. V.; Holguin, F.; Hong, Y.; Luepker, R. V.; Mittleman, M. A.; Peters, A.; Siscovick, D.; Smith, S. C.; Whitsel, L.; Kaufman, J. D. *Circulation*. 2010.
(7) Buda, F.; Ensing, B.; Gribnau, M. C. M.; Baerends, E. J. *Chem. - A Eur. J.* **2003**, *9* (14), 3436–3444.
(8) Cho, A.; Sioutas, C.; Miguel, A. H.; Kumagai, Y.; Schmita, D. A.; Singh, M.; Froines, J. R. *Environ. Res.* **2005**, *99*, 40–47.
(9) Ess, M. N.; Ferry, D.; Kireeva, E. D.; Niessner, R.; Ouf, F. X.; Ivleva, N. P. *Carbon N. Y.* **2016**, *105*, 572–585.
(10) Faiola, C.; Johansen, A. M.; Rybka, S.; Nieber, A.; Thomas, C.; Bryner, S.; Johnston, J.; Engelhard, M.; Nachimuthu, P.; Owens, K. S. *Aerosol Sci. Technol.* **2011**, *45* (9), 1109–1122.
(11) Ferreira, E. H.; Moutinho, M. V. O.; Stavale, F.; Lucchese, M. M.; Capaz, R. B.; Achete, C. A.; Jorio, A. *Phys. Rev. B - Condens. Matter Mater. Phys.* **2010**, *82* (12), 1–9.
(12) Gaffney, J. S.; Marley, N. A.; Smith, K. J. *J. Phys. Chem. A* **2015**, *119* (19), 4524–4532.
(13) Herner, J. D.; Green, P. G.; Kleeman, M. J. *Environ. Sci. Technol.* **2006**, *40* (6), 1925–1933.
(14) Jacobson, M. Z. *J. Geophys. Res. Atmos.* **2010**, *115* (14).
(15) Long, C. M.; Nascarella, M. A.; Valberg, P. A. *Environ. Pollut.* **2013**, *181*, 271–286.
(16) Muller, J. O.; Schogl, R. *Catal. Today* **2006**, 1–2.
(17) Niranjan, R.; Thakur, A. K. *Front. Immunol.* **2017**, *8* (JUN).
(18) Peng, R. D.; Bell, M. L.; Geyh, A. S.; McDermott, A.; Zeger, S. L.; Samet, J. M.; Dominici, F. *Environmental Health Perspectives*. 2009, pp 957–963.
(19) Rappazzo, K. M.; Daniels, J. L.; Messer, L. C.; Poole, C.; Lobdell, D. T. *Environ. Health Perspect.* **2015**, *123* (10), 1059–1065.
(20) Sadezky, A.; Muckenhuber, H.; Grothe, H.; Niessner, R.; Pöschl, U. *Carbon N. Y.* **2005**, *43* (8), 1731–1742.
(21) Samara, C.; Voutsa, D.; Kouras, A.; Eleftheriadis, K.; Maggos, T.; Saraga, D.; Petrakakis, M. *Environ. Sci. Pollut. Res.* **2014**, *21* (3), 1769–1785.

CHAPTER V

CONCLUSION

A relatively simple fluorometric GSH assay was optimized for studying the oxidative potential of PM in PBS with an emphasis on carbonaceous nanoparticles, including diesel soot. However, this method is transferrable to $PM_{2.5}$ analysis. The reaction of GSH with OPA is specific in this system, with signal detection and quantitation limits of 0.032 and 0.49 µM GSH, respectively. The dynamic calibration range extended to 100 µM GSH, which was the maximum GSH concentration added to PM slurries. Highly reproducible triplicate runs of all PM samples resulted in pseudo first order reaction rates with respect to GSH consumption. This method provides a simple assay to gather robust complementary information that can help shed light on the particle characteristics that lead to the oxidation of the GSH, a key player in cellular health.

Oxidative capacity for one standard diesel sample and six other surrogate CNP samples was determined by GSH consumption and showed that soot with varying physicochemical properties have unique oxidative potentials, as described by their pseudo first order rate constants. Physical and chemical properties were correlated with rate constants for consumption of GSH by CNP and it was found that there is no direct correlation between pseudo first order rate constants and any one physicochemical property. Consumption rates of GSH increased significantly after CNP samples were heat-treated at 700 ºC under N_2. TGA analysis provided insight on chemical composition of soot particles and leads to further investigation of the microstructures of particles to determine their elemental carbon (EC) make-up by Raman microspectroscopy. Multilinear regression analysis modeled pseudo first order rate constant, k', after heat-treatment with both the sum of total transition metals (Ti-Zn) and the loss in mass after

heat treating to 700 ˚C as variables, resulting in an R^2 value of 0.708. This confirms that the PAHs present inhibit the reactivity of CNP toward GSH and that EC may be the driving force behind particle toxicity. This is to be further investigated by Raman microspectroscopy to study the change in microstructure after heat-treatment and then correlated with the current data set. Ultimately, the understanding of particle toxicity was contributed to by the findings of this work as research continues to uncover what drives CNP toxicity.

REFERENCES

(1) Antiñolo, M.; Willis, M. D.; Zhou, S.; Abbatt, J. P. D. *Nat. Commun.* **2015**, *6*, 6812.
(2) Atkinson, R. W.; Mills, I. C.; Walton, H. A.; Anderson, H. R. *J. Expo. Sci. Environ. Epidemiol.* **2015**.
(3) Ayres, J. G.; Borm, P.; Cassee, F. R.; Castranova, V.; Donaldson, K.; Ghio, A.; Harrison, R. M.; Hider, R.; Kelly, F.; Kooter, I. M.; Marano, F.; Maynard, R. L.; Mudway, I.; Nel, A.; Sioutas, C.; Smith, S.; Baeza-Squiban, A.; Cho, A.; Duggan, S.; Froines, J. In *Inhalation Toxicology*; 2008; pp 75–99.
(4) B. Z. Simkhovich, M. T. Kleinman, R. A. K. *J. Am. Coll. Cardinology* **2008**, *52* (9), 719–726.
(5) Bell, M. L.; Ebisu, K.; Peng, R. D.; Samet, J. M.; Dominici, F. *American Journal of Respiratory and Critical Care Medicine*. 2009, pp 1115–1120.
(6) Benson, J. R.; Hare, P. E. *Proc. Natl. Acad. Sci.* **1975**, *72* (2), 619–622.
(7) Bond, T. C.; Sun, K. *Environ. Sci. Technol.* **2005**, *39* (16), 5921–5926.
(8) Borsook, H.; Keighley, G. *Proc. Natl. Acad. Sci. U. S. A.* **1933**, *19* (Vitamin C), 875–878.
(9) Bredin, A.; Larcher, A.; Mullins, B. *Tribol. Int.* **2011**, *44* (12), 1642–1650.
(10) Brook, R. D.; Rajagopalan, S.; Pope, C. A.; Brook, J. R.; Bhatnagar, A.; Diez-Roux, A. V.; Holguin, F.; Hong, Y.; Luepker, R. V.; Mittleman, M. A.; Peters, A.; Siscovick, D.; Smith, S. C.; Whitsel, L.; Kaufman, J. D. *Circulation*. 2010.
(11) Buda, F.; Ensing, B.; Gribnau, M. C. M.; Baerends, E. J. *Chem. - A Eur. J.* **2003**, *9* (14), 3436–3444.
(12) Charrier, J. G.; Anastasio, C. **2012**, 9321–9333.
(13) Cho, A.; Sioutas, C.; Miguel, A. H.; Kumagai, Y.; Schmita, D. A.; Singh, M.; Froines, J. R. *Environ. Res.* **2005**, *99*, 40–47.
(14) Cleland, W. W. *Biochemistry* **1964**, *4*, 480–482.
(15) Cohn, V. H.; Lyle, J. *Anal. Biochem.* **1966**, *14* (3), 434–440.
(16) EPA. *BC Emissions.pdf*; 2012.
(17) Ess, M. N.; Ferry, D.; Kireeva, E. D.; Niessner, R.; Ouf, F. X.; Ivleva, N. P. *Carbon N. Y.* **2016**, *105*, 572–585.
(18) Faiola, C.; Johansen, A. M.; Rybka, S.; Nieber, A.; Thomas, C.; Bryner, S.; Johnston, J.; Engelhard, M.; Nachimuthu, P.; Owens, K. S. *Aerosol Sci. Technol.* **2011**, *45* (9), 1109–1122.
(19) Fang, T.; Verma, V.; T Bates, J.; Abrams, J.; Klein, M.; Strickland, J. M.; Sarnat, E. S.; Chang, H. H.; Mulholland, A. J.; Tolbert, E. P.; Russell, G. A.; Weber, J. R. *Atmos. Chem. Phys.* **2016**, *16*, 3865–3879.
(20) Ferreira, E. H.; Moutinho, M. V. O.; Stavale, F.; Lucchese, M. M.; Capaz, R. B.; Achete, C. A.; Jorio, A. *Phys. Rev. B - Condens. Matter Mater. Phys.* **2010**, *82* (12), 1–9.
(21) Gaffney, J. S.; Marley, N. A.; Smith, K. J. *J. Phys. Chem. A* **2015**, *119* (19), 4524–4532.
(22) Galant, N. J.; Wang, H.; Lee, D. J. R.; Mucsi, Z.; Setiadi, D. H.; Viskolcz, B.; Csizmadia, I. G. *J. Phys. Chem. A* **2009**, *113* (32), 9138–9149.
(23) Garcia-Fernandez, C.; Picaud, S.; Rayez, M. T.; Rayez, J. C.; Rubayo-Soneira, J. *J. Phys. Chem. A* **2014**, *118* (8), 1443–1450.
(24) Glasauer, A.; N. S. Chandel. *Curr. Biol. 23* (3), R100–R102.
(25) Grahame, T. J.; Klemm, R.; Schlesinger, R. B. *J. Air Waste Manage. Assoc.* **2014**, *64*, 620–660.

(26) Herner, J. D.; Green, P. G.; Kleeman, M. J. *Environ. Sci. Technol.* **2006**, *40* (6), 1925–1933.
(27) Hiroi, M.; Ogihara, T.; Hirano, K.; Hasegawa, M.; Morinobu, T.; Tamai, H.; Niki, E. *Free Radic. Biol. Med.* **2005**, *38*, 1057–1072.
(28) Hissin, P. J.; Hilf, R. *Anal. Biochem.* **1976**, *74* (1), 214–226.
(29) Hu, H.; Liang, Y.; Li, S.; Guo, Q.; Wu, C. *J. Anal. Methods Chem.* **2014**.
(30) Jacobson, M. Z. *J. Geophys. Res. Atmos.* **2010**, *115* (14).
(31) Kandar, R.; Vrbová, M.; Andová, J. Č. *J. Liq. Chromatogr. Relat. Technol.* **2013**, *36*, 2013–2028.
(32) Krzyżanowski, D.; Bartosz, G.; Grzelak, A. *Free Radic. Biol. Med.* **2014**, *76*, 47–52.
(33) Liggio, J.; Gordon, M.; Smallwood, G.; Li, S. M.; Stroud, C.; Staebler, R.; Lu, G.; Lee, P.; Taylor, B.; Brook, J. R. *Environ. Sci. Technol.* **2012**, *46* (9), 4819–4828.
(34) Long, C. M.; Nascarella, M. A.; Valberg, P. A. *Environ. Pollut.* **2013**, *181*, 271–286.
(35) McWhinney, R. D.; Badali, K.; Liggio, J.; Li, S.-M.; Abbatt, J. P. D. *Environ. Sci. Technol.* **2013**, *47* (7), 3362–3369.
(36) Millis, K. K.; Weaver, K. H.; Rabenstein, D. L. *J. Org. Chem.* **1993**, *58* (15), 4144–4146.
(37) Muller, J. O.; Schogl, R. *Catal. Today* **2006**, 1–2.
(38) Niranjan, R.; Thakur, A. K. *Front. Immunol.* **2017**, *8* (JUN).
(39) Peng, R. D.; Bell, M. L.; Geyh, A. S.; McDermott, A.; Zeger, S. L.; Samet, J. M.; Dominici, F. *Environmental Health Perspectives*. 2009, pp 957–963.
(40) Penn, A.; Murphy, G.; Barker, S.; Henk, W.; Penn, L. *Environ. Health Perspect.* **2005**, *113* (8), 956–963.
(41) Rappazzo, K. M.; Daniels, J. L.; Messer, L. C.; Poole, C.; Lobdell, D. T. *Environ. Health Perspect.* **2015**, *123* (10), 1059–1065.
(42) Ristovski, Z. D.; Miljevic, B.; Surawski, N. C.; Morawska, L.; Fong, K. M.; Goh, F.; Yang, I. A. *Respirology*. 2012, pp 201–212.
(43) Roušar, T.; Kučera, O.; Lotková, H.; Červinková, Z. *Anal. Biochem.* **2012**, *423* (2), 236–240.
(44) Sadezky, A.; Muckenhuber, H.; Grothe, H.; Niessner, R.; Pöschl, U. *Carbon N. Y.* **2005**, *43* (8), 1731–1742.
(45) Samara, C.; Voutsa, D.; Kouras, A.; Eleftheriadis, K.; Maggos, T.; Saraga, D.; Petrakakis, M. *Environ. Sci. Pollut. Res.* **2014**, *21* (3), 1769–1785.
(46) Schafer, F.; Buettner, G. *Free Radic. Biol. Med.* **2001**, *30*, 1191–1212.
(47) Sharma, H. N.; Pahalagedara, L.; Joshi, A.; Suib, S. L.; Mhadeshwar, A. B. *Energy and fuels* **2012**, *26* (2), 5613–5625.
(48) Tsai, J.-H.; Lin, J.-H.; Yao, Y.-C.; Chiang, H.-L. *Aerosol Air Qual. Res.* **2012**, *12*, 263–274.
(49) Tuet, W. Y.; Chen, Y.; Xu, L.; Fok, S.; Gao, D.; Weber, R. J.; Ng, N. L. *Atmos. Chem. Phys.* **2017**, *17* (2), 839–853.
(50) Verma, V.; Fang, T.; Guo, H.; King, L.; Bates, J. T.; Peltier, R. E.; Edgerton, E.; Russell, A. G.; Weber, R. J. **2014**, 12915–12930.
(51) W. H. Watson, Y. Chen, D. P. J. *Thiol Metab. Redox Regul. Cell. Funct.* **2003**, *17* (1–4), 328–331.
(52) Wood, P. M. *Biochem. J.* **1988**, *253* (1), 287–289.
(53) Xiong, Q.; Yu, H.; Wang, R.; Wei, J.; Verma, V. *Environ. Sci. Technol.* **2017**.

(54) Yang, F.; Tan, J.; Zhao, Q.; Du, Z.; He, K.; Ma, Y.; Duan, F.; Chen, G.; Zhao, Q. *Atmos. Chem. Phys.* **2011**, *11*, 5207–5219.

APPENDIX A – MORPHOLOGIES

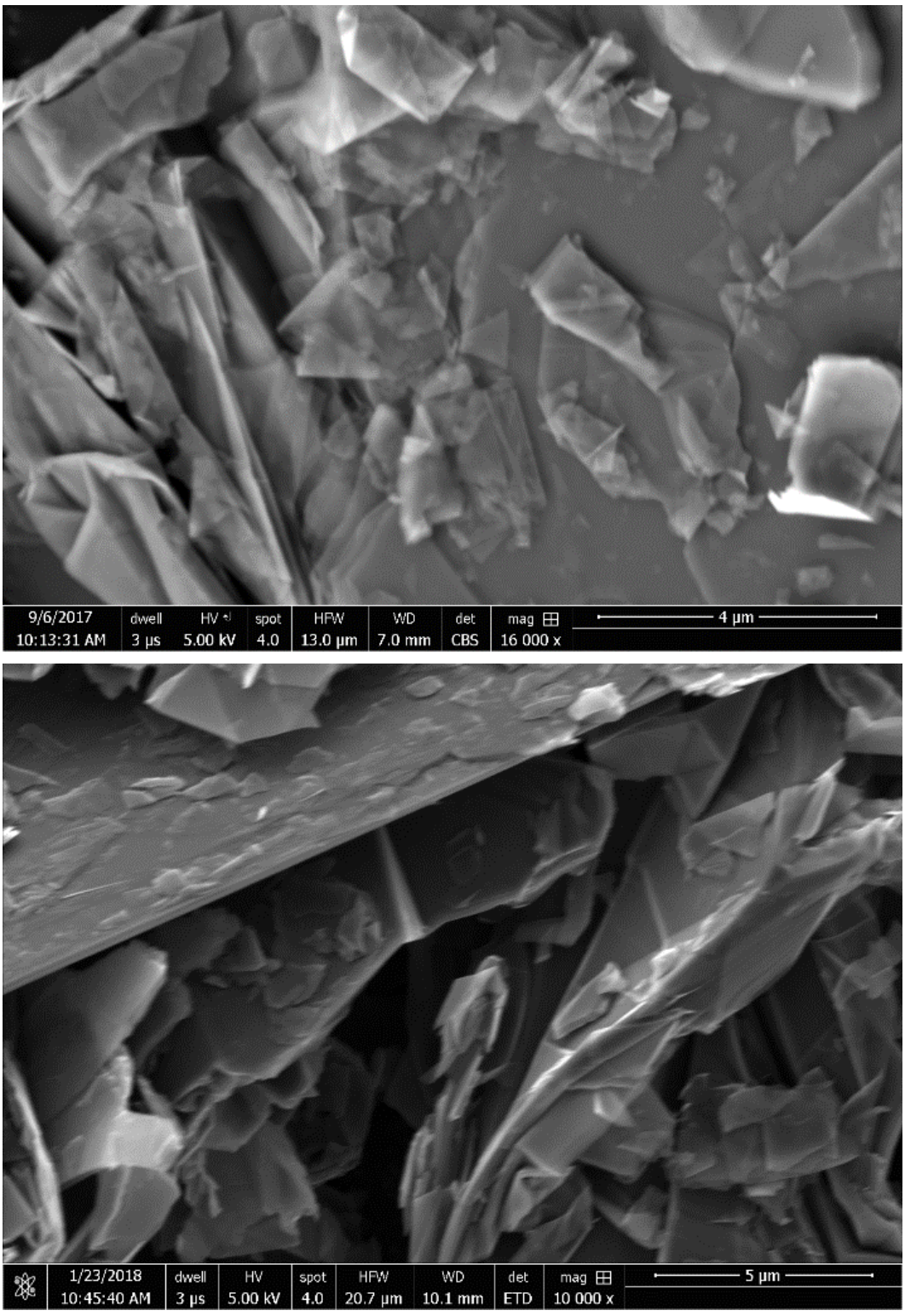

Figure 21 Graphite untreated (top) and heat-treated (bottom)

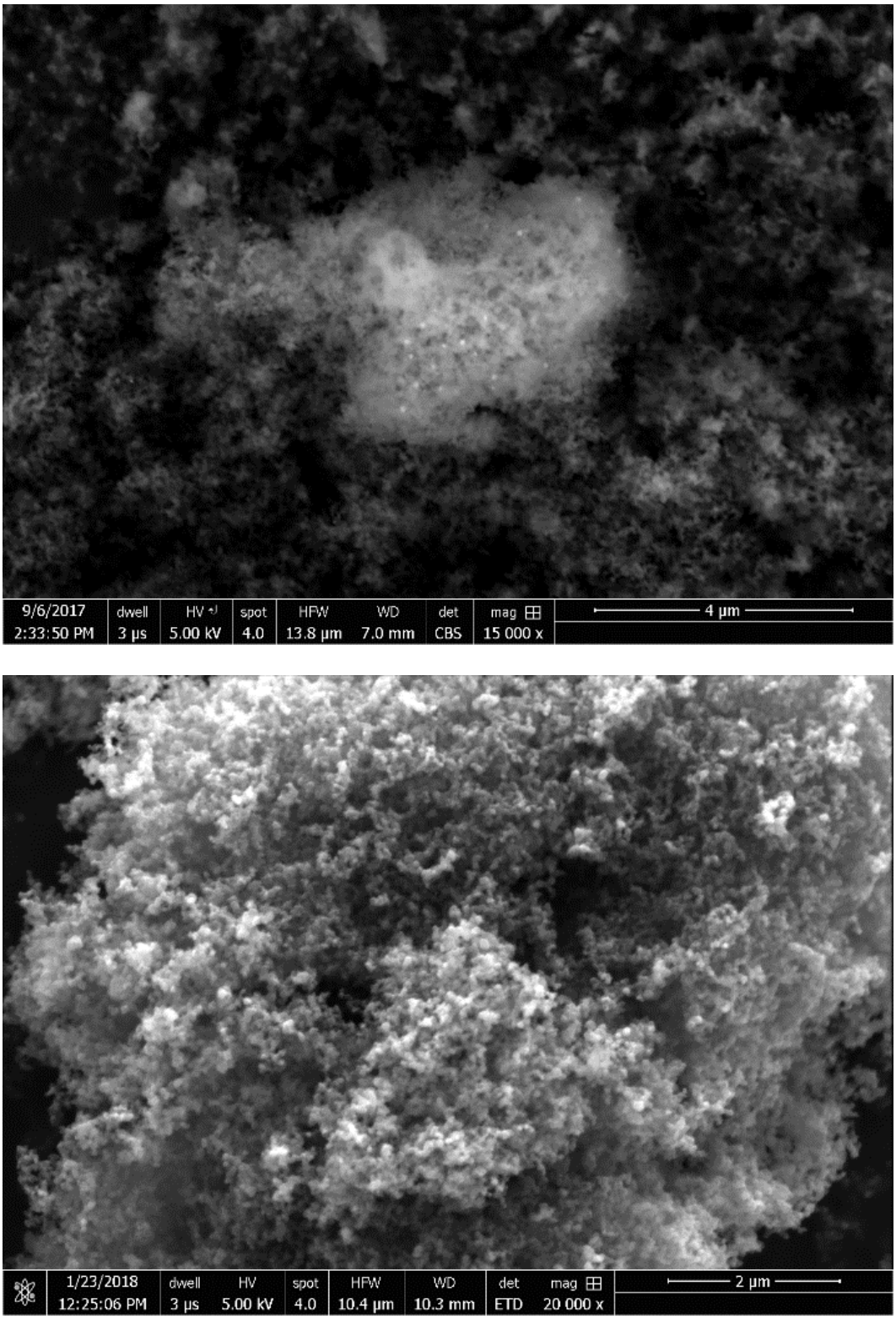

Figure 22 XE2 untreated (top) and heat-treated (bottom)

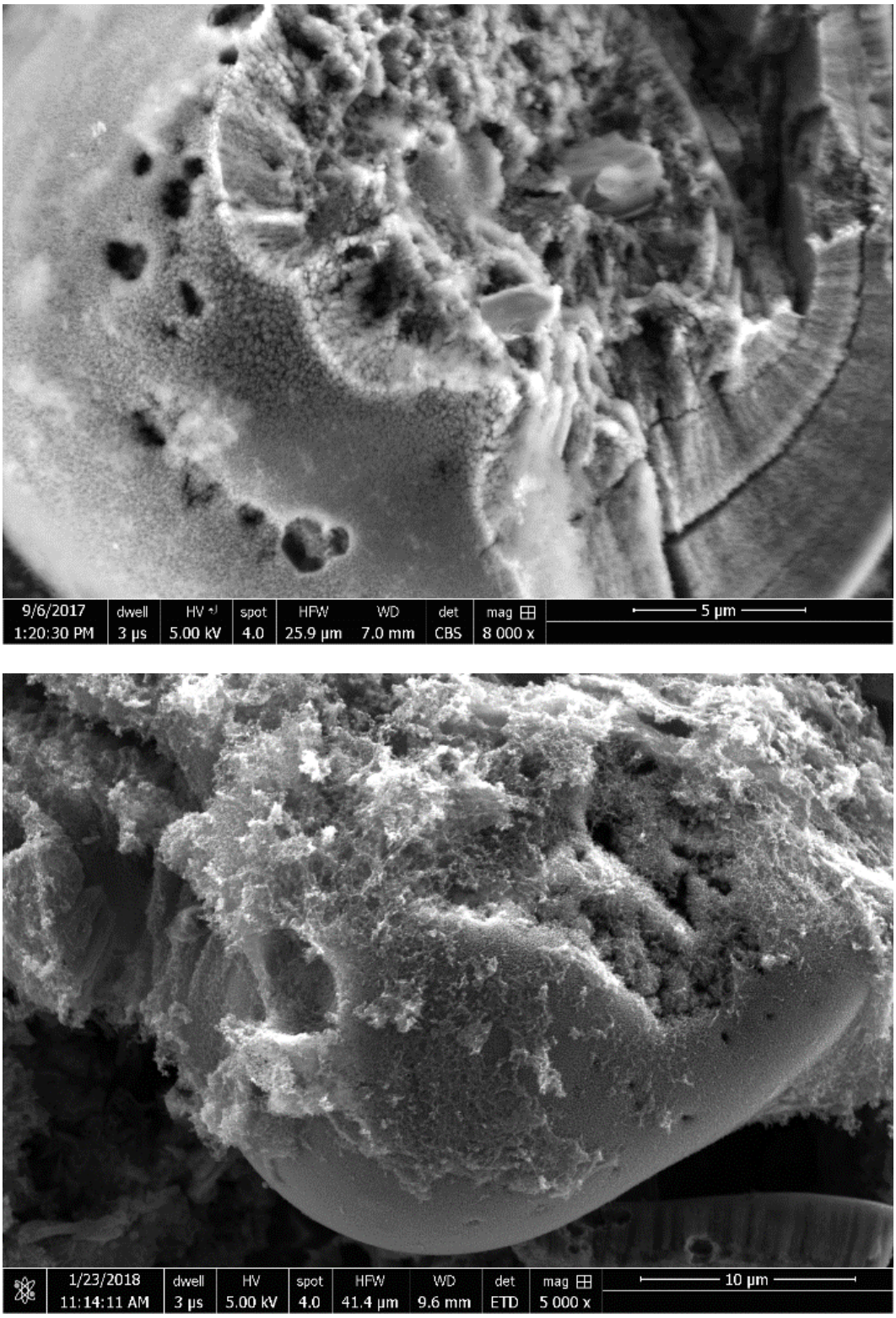

Figure 23 GfG untreated (left) and heat-treated (right)

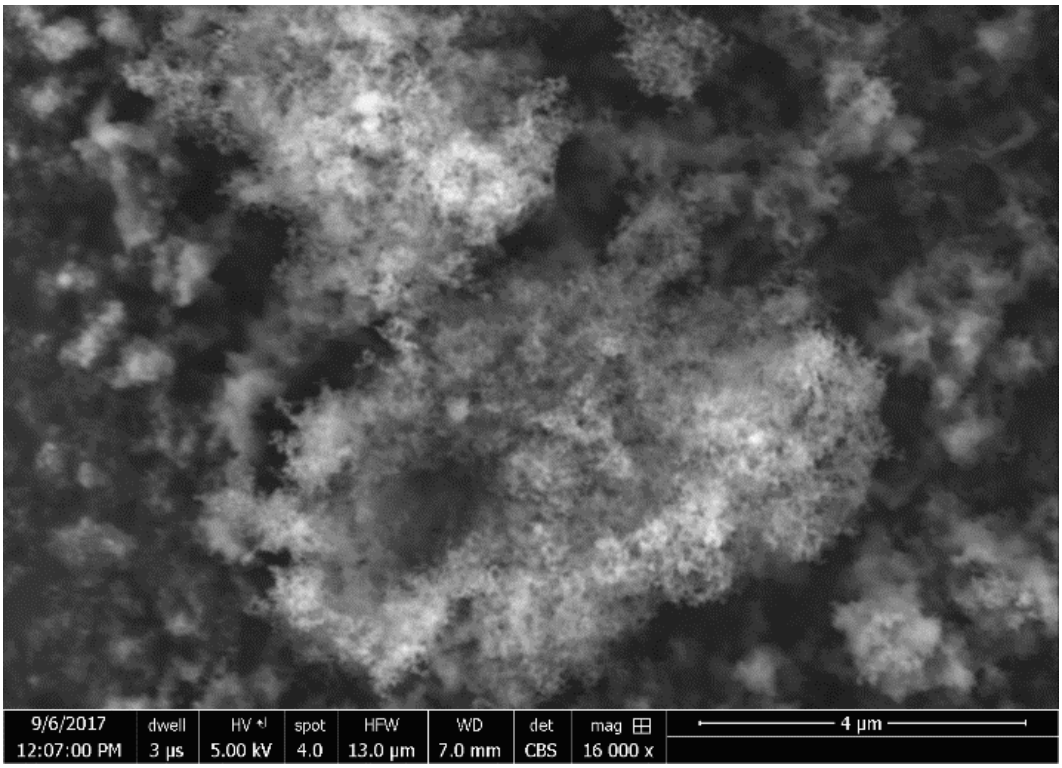

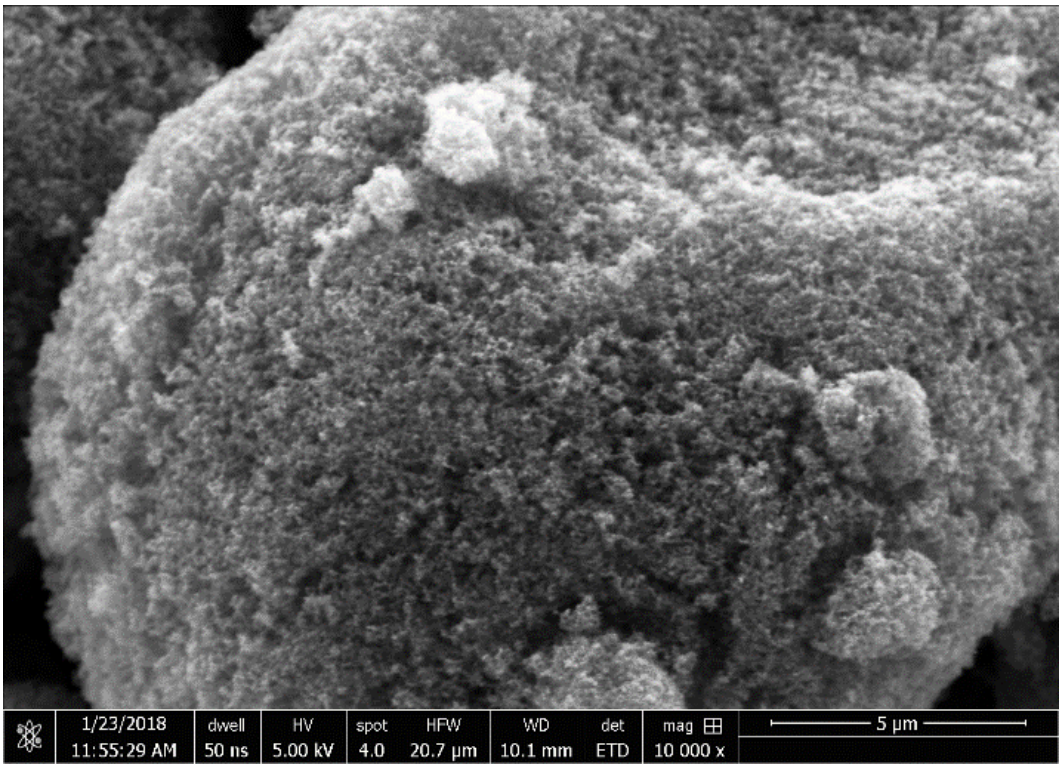

Figure 24 NIST untreated (top) and heat-treated (bottom)

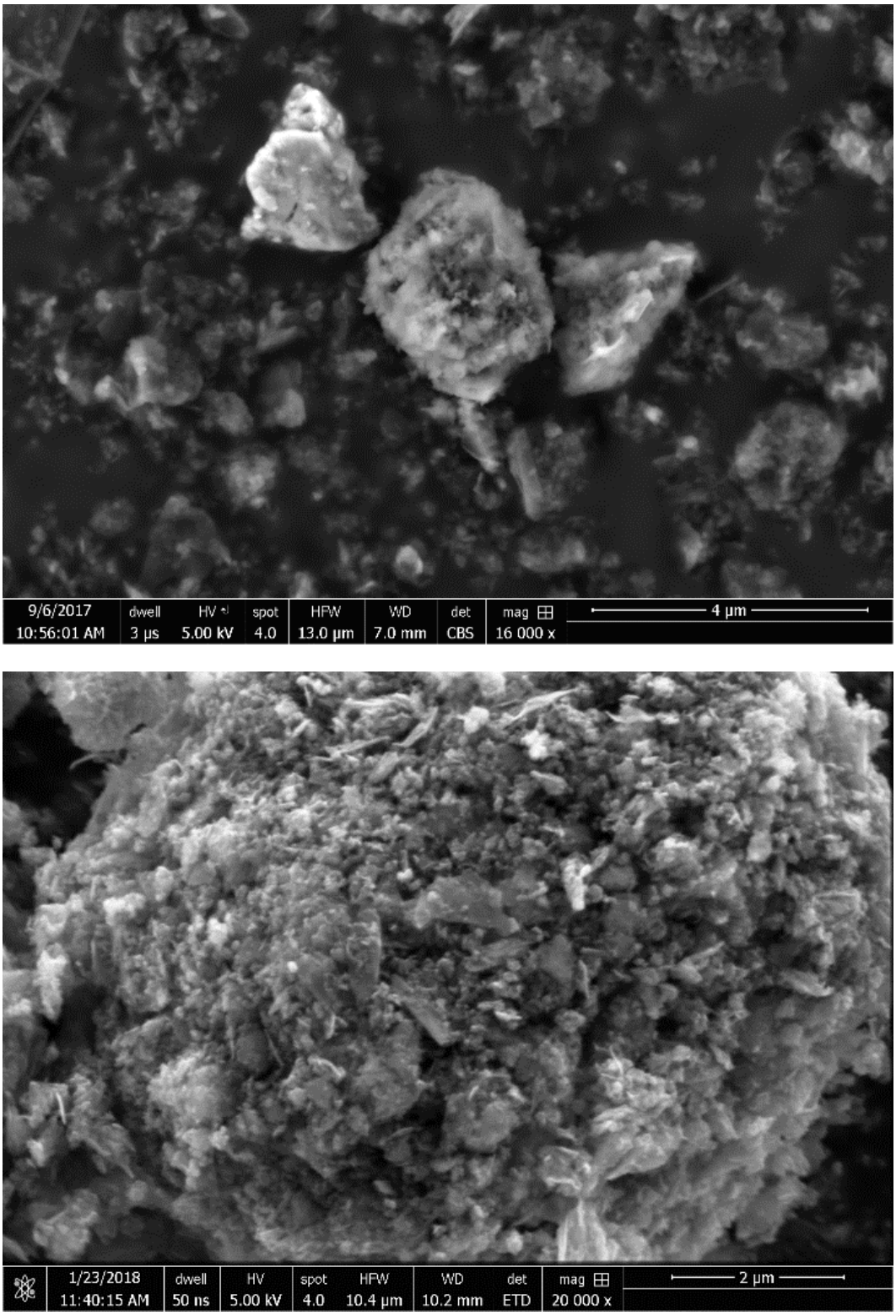

Figure 25 Graphene untreated (top) and heat-treated (bottom)

5

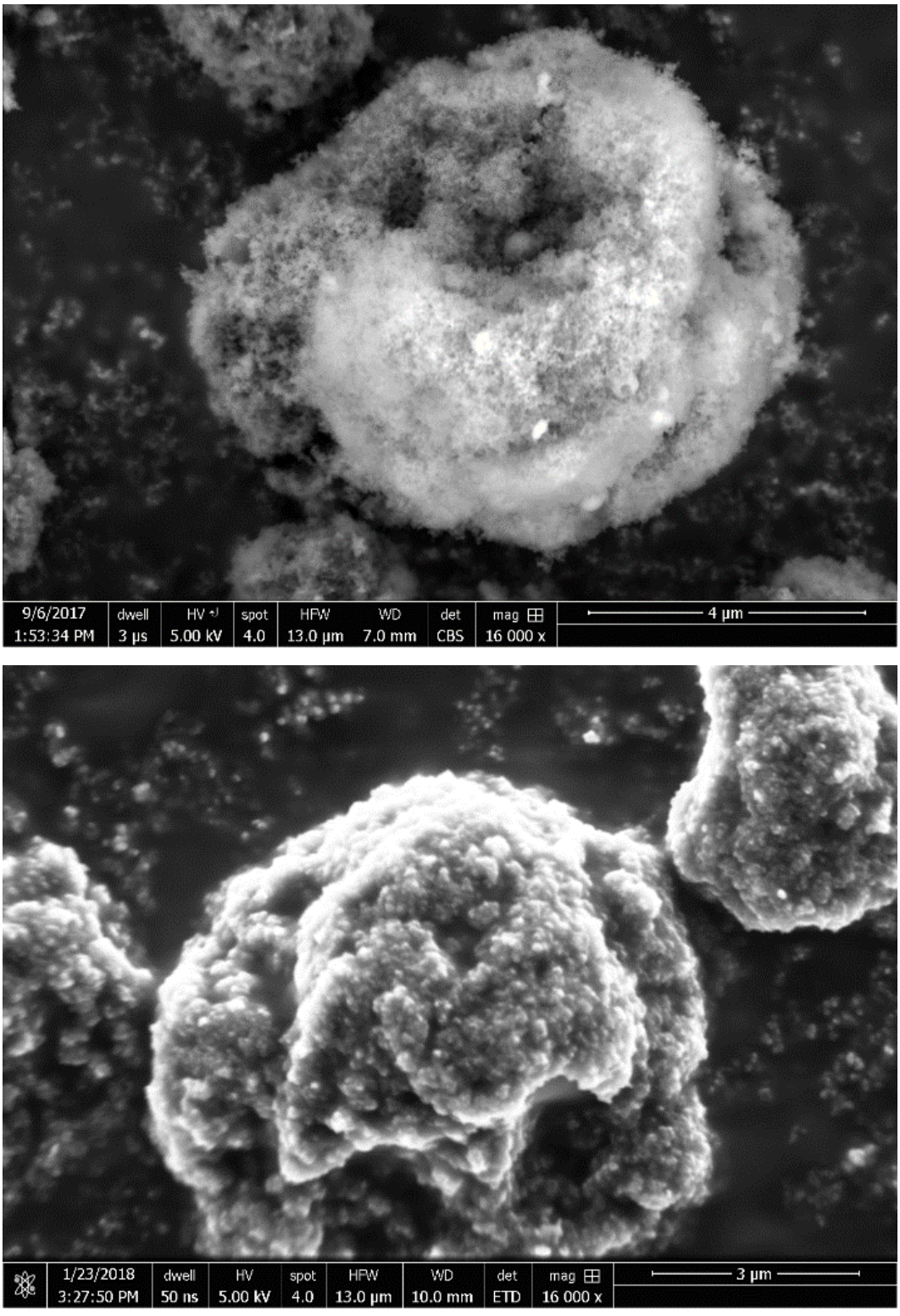

Figure 26 P90 untreated (top) and heat-treated (bottom)

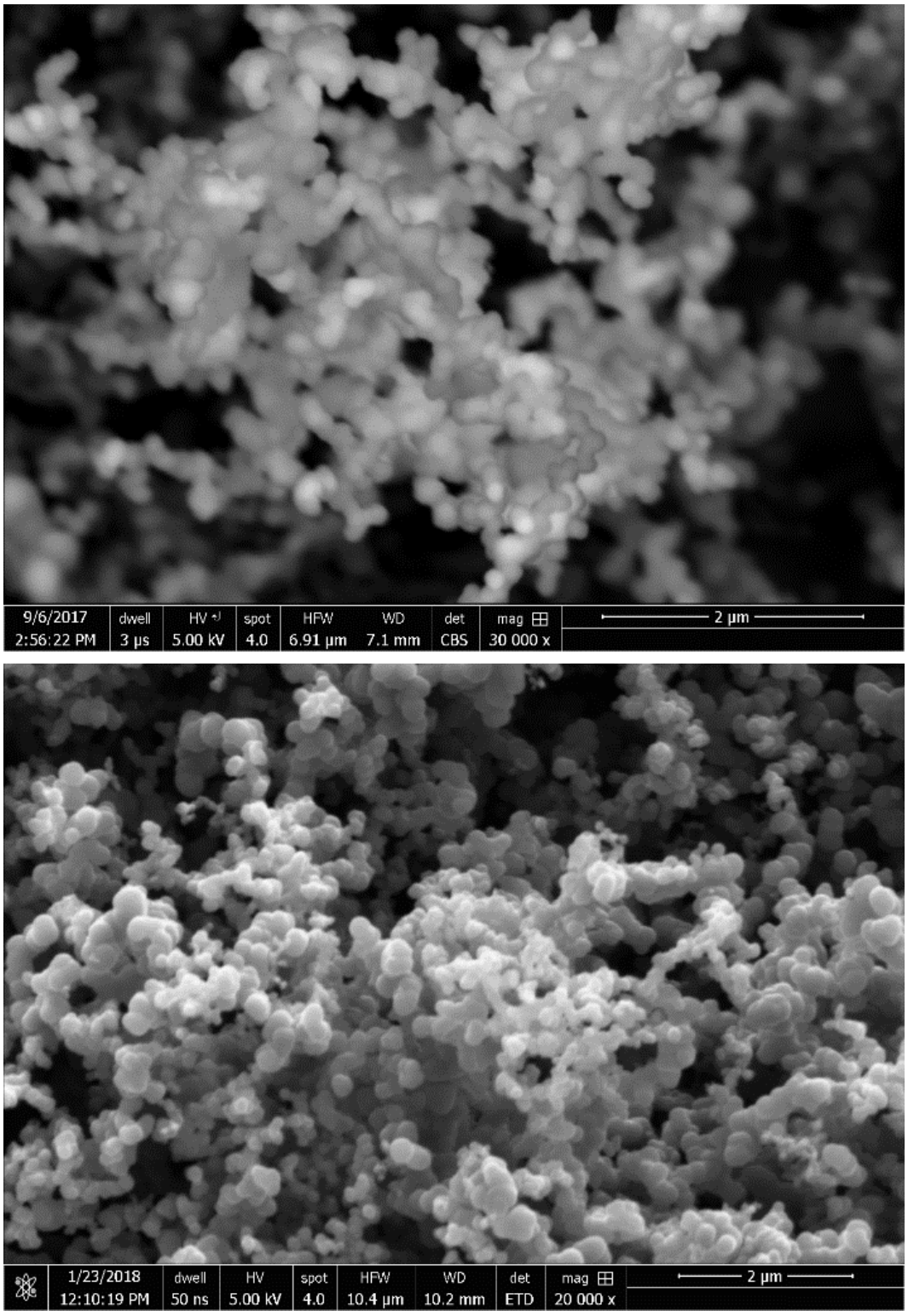

Figure 27 F101 untreated (top) and heat-treated (bottom)

APPENDIX B – ELEMENTAL ANALYSIS

The following EDS spectra determine elements present in CNP samples. All samples show a dominating carbon peak, as expected. A few samples show trace metals consistent with ICP-MS findings, such as vanadium in XE2. Each set of spectra are labeled by a header with the sample ID.

F101

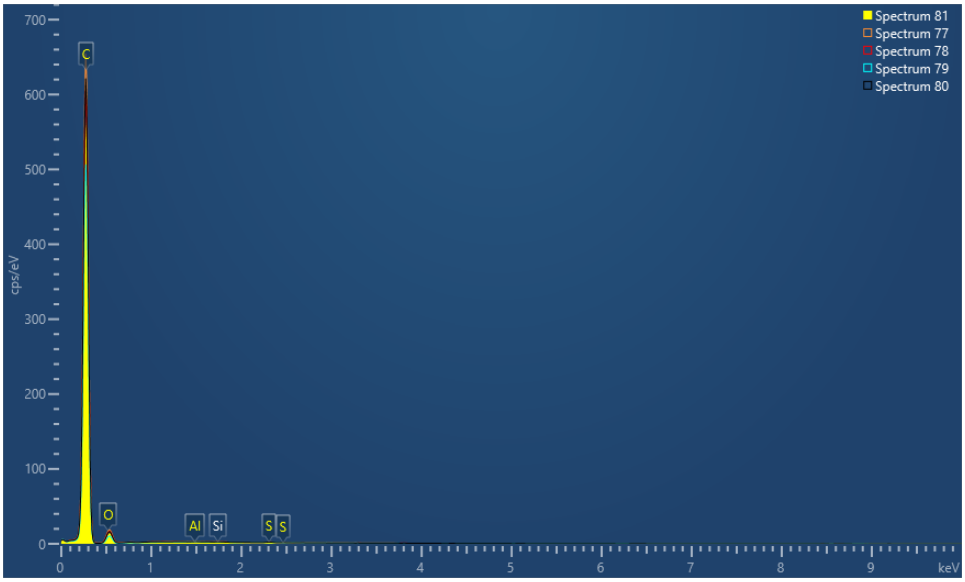

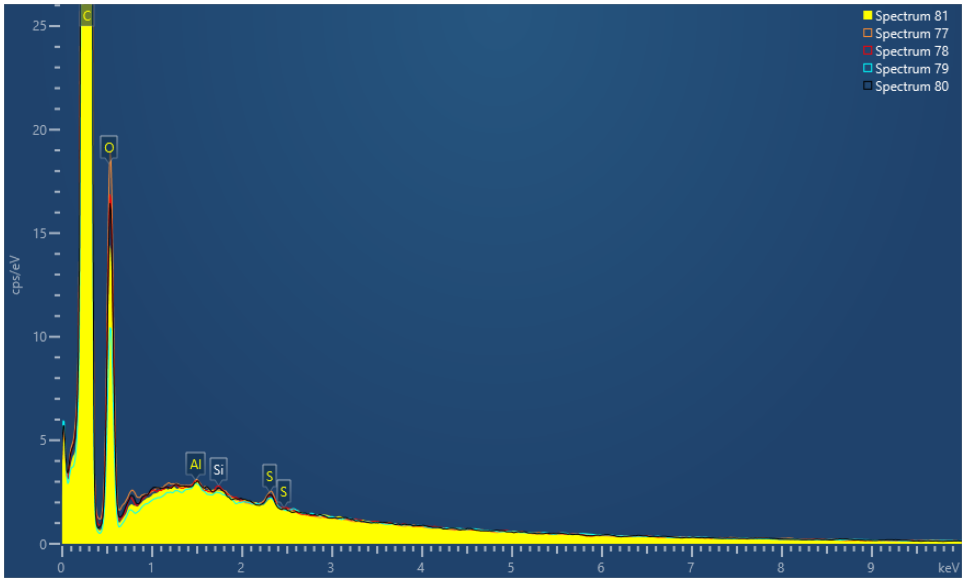

NIST


Spectrum 22
Spectrum 15
Spectrum 16
Spectrum 17
Spectrum 18
Spectrum 19
Spectrum 20
Spectrum 21
cps/eV
keV
C
O
Al
Si
S

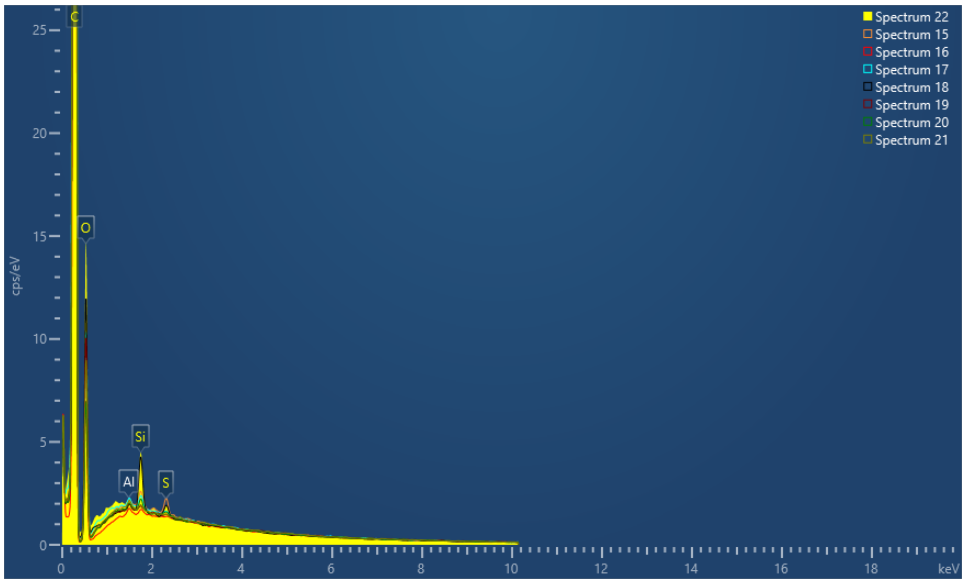
Spectrum 22
Spectrum 15
Spectrum 16
Spectrum 17
Spectrum 18
Spectrum 19
Spectrum 20
Spectrum 21
cps/eV
keV
C
O
Si
Al
S

GfG

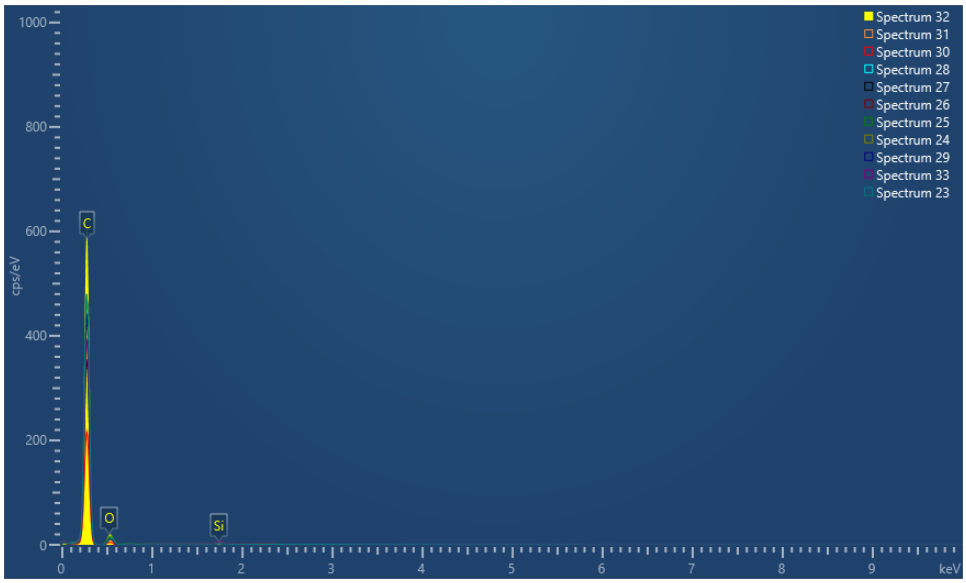
Spectrum 32
Spectrum 31
Spectrum 30
Spectrum 28
Spectrum 27
Spectrum 26
Spectrum 25
Spectrum 24
Spectrum 29
Spectrum 33
Spectrum 23
cps/eV
C
O
Si
keV

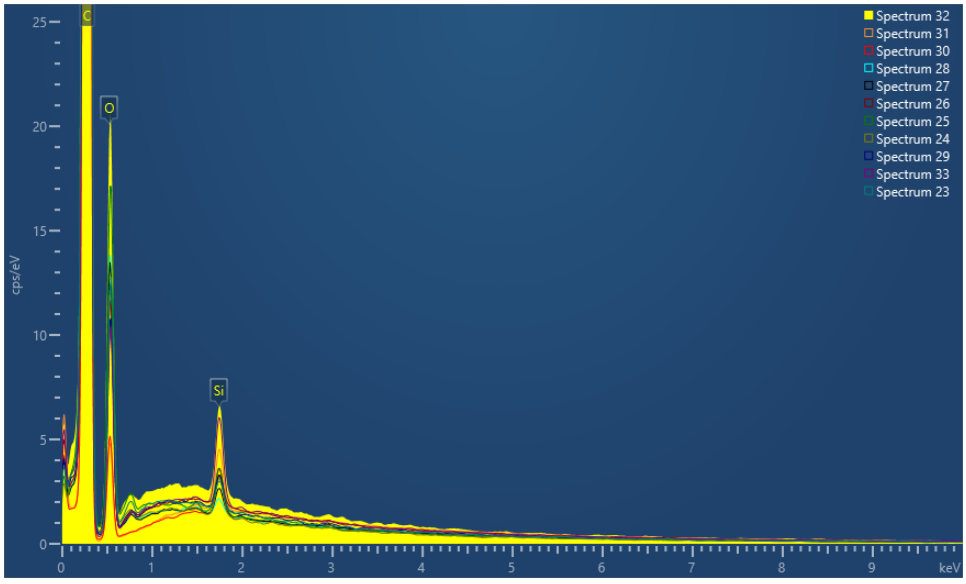
Spectrum 32
Spectrum 31
Spectrum 30
Spectrum 28
Spectrum 27
Spectrum 26
Spectrum 25
Spectrum 24
Spectrum 29
Spectrum 33
Spectrum 23
cps/eV
C
O
Si
keV

XE2

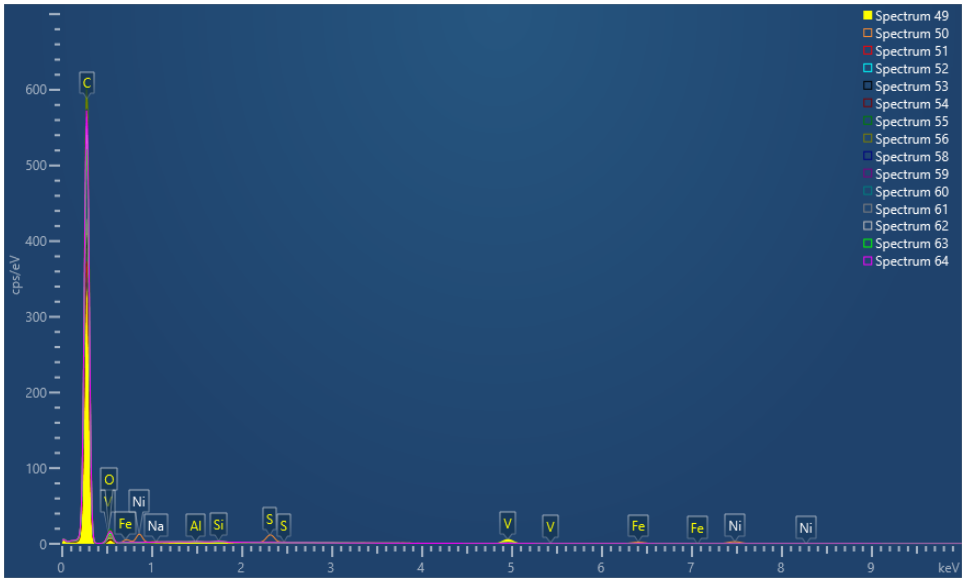
Spectrum 49
Spectrum 50
Spectrum 51
Spectrum 52
Spectrum 53
Spectrum 54
Spectrum 55
Spectrum 56
Spectrum 58
Spectrum 59
Spectrum 60
Spectrum 61
Spectrum 62
Spectrum 63
Spectrum 64
cps/eV
keV
C
O
V
Ni
Fe
Na
Al
Si
S
V
Fe
Fe
Ni
Ni

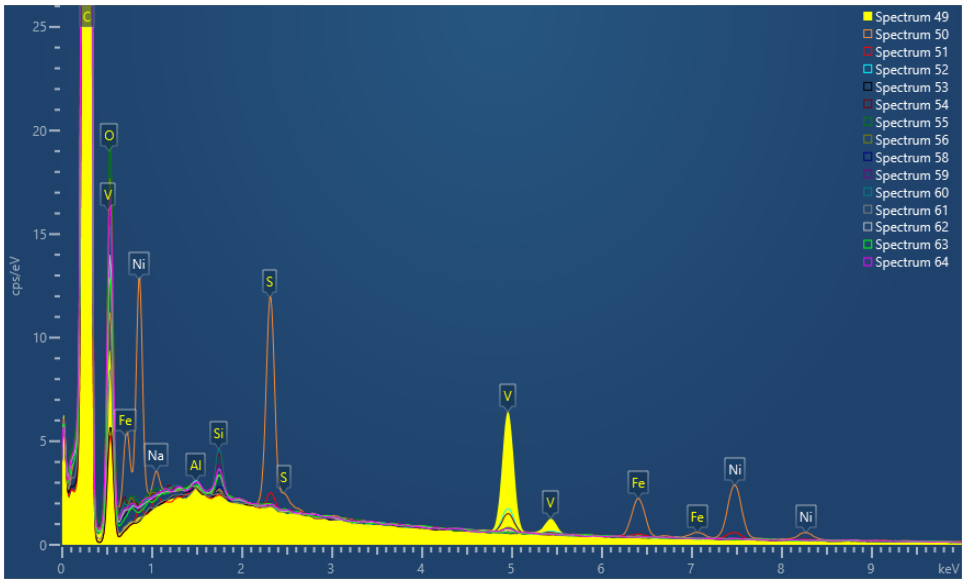
Spectrum 49
Spectrum 50
Spectrum 51
Spectrum 52
Spectrum 53
Spectrum 54
Spectrum 55
Spectrum 56
Spectrum 58
Spectrum 59
Spectrum 60
Spectrum 61
Spectrum 62
Spectrum 63
Spectrum 64
cps/eV
keV
C
O
V
Ni
S
Fe
Na
Al
Si
S
V
Fe
Fe
Ni
Ni

P90

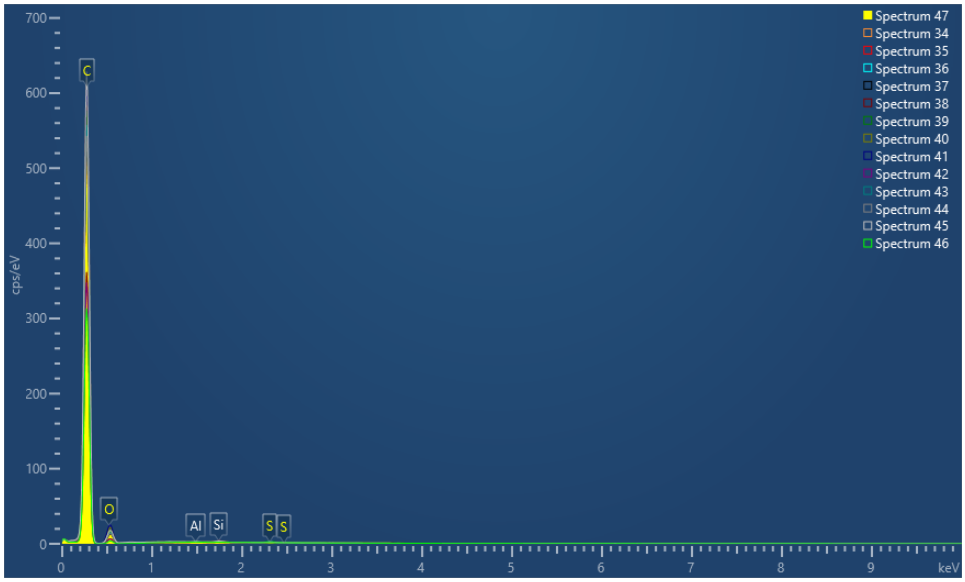
Spectrum 47
Spectrum 34
Spectrum 35
Spectrum 36
Spectrum 37
Spectrum 38
Spectrum 39
Spectrum 40
Spectrum 41
Spectrum 42
Spectrum 43
Spectrum 44
Spectrum 45
Spectrum 46
cps/eV
keV
C
O
Al
Si
S
S

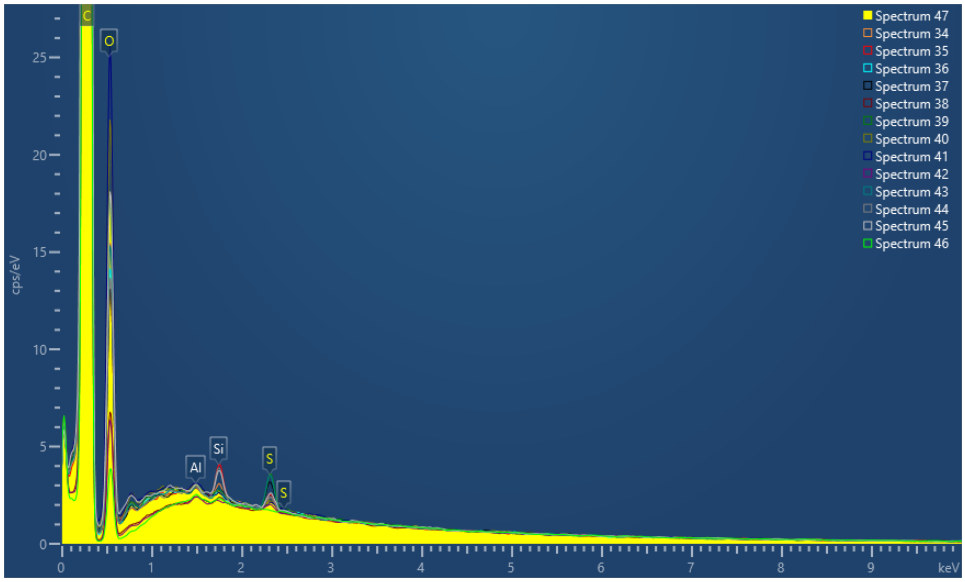
Spectrum 47
Spectrum 34
Spectrum 35
Spectrum 36
Spectrum 37
Spectrum 38
Spectrum 39
Spectrum 40
Spectrum 41
Spectrum 42
Spectrum 43
Spectrum 44
Spectrum 45
Spectrum 46
cps/eV
keV
C
O
Al
Si
S
S

Graphite


Spectrum 8
Spectrum 1
Spectrum 2
Spectrum 3
Spectrum 4
Spectrum 5
Spectrum 6
Spectrum 7
C
O
Si
cps/eV
keV

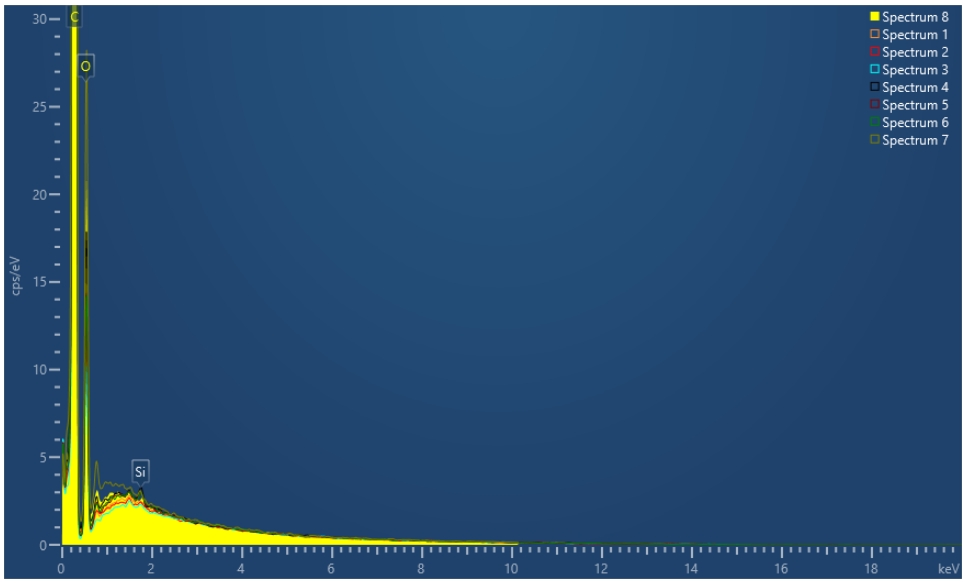
Spectrum 8
Spectrum 1
Spectrum 2
Spectrum 3
Spectrum 4
Spectrum 5
Spectrum 6
Spectrum 7
C
O
Si
cps/eV
keV

Graphene

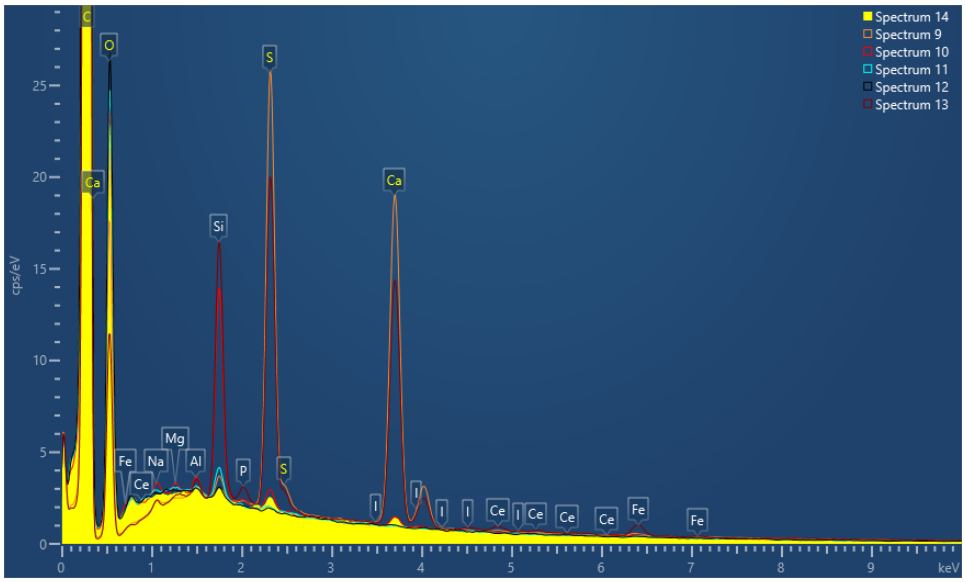
Spectrum 14
Spectrum 9
Spectrum 10
Spectrum 11
Spectrum 12
Spectrum 13
C
O
Ca
Si
S
Ca
Mg
Fe
Na
Al
Ce
P
S
I
I
I
I
Ce
I
Ce
Ce
Ce
Fe
Fe
cps/eV
keV